Ore Geology Reviews 73 (2016) 104–126

Contents lists available at ScienceDirect

Ore Geology Reviews

journal homepage: www.elsevier.com/locate/oregeorev

The Patricia Zn–Pb–Ag epithermal ore deposit: An uncommon type of mineralization in northeastern Chile

Darío Chinchilla [a,b,*], Lorena Ortega [a], Rubén Piña [a], Raúl Merinero [a], Daniel Moncada [c], Robert J. Bodnar [d], Cecilio Quesada [a], Antonio Valverde [e], Rosario Lunar [a,b]

[a] Departamento de Cristalografía y Mineralogía, Facultad de Ciencias Geológicas, Universidad Complutense de Madrid, C/ José Antonio Novais, s/n., 28040, Madrid, Spain
[b] Instituto de Geociencias IGEO (UCM-CISC), C/ José Antonio Novais, s/n., 28040 Madrid, Spain
[c] Departamento de Geología and Andean Geothermal Center of Excellence (CEGA), Universidad de Chile, Plaza Ercilla 803, Santiago, Chile
[d] Department of Geosciences, Virginia Tech, Blacksburg, VA 24061, United States
[e] Herencia Resources Plc. Compañía minera Paguanta, Santiago de Chile, Chile

ARTICLE INFO

Article history:
Received 4 August 2015
Received in revised form 21 October 2015
Accepted 23 October 2015
Available online 24 October 2015

Keywords:
Intermediate-sulfidation
Ag-sulfosalts
Open-space filling
Polymetallic epithermal
Strike-slip duplex
Domeyko fault system
Metallogenic belt

ABSTRACT

The Patricia ore deposit represents an unusual example of economic Zn–Pb–Ag mineralization at the northernmost end of the Late Eocene–Oligocene metallogenic belt in Chile. It is hosted by volcano-sedimentary units, which are typically tuffaceous and andesitic breccias. The ore body consists of a set of subvertical E-W vein systems developed under a sinistral strike-slip regime that included transtensive domains with generalized extensional structures where the ores were deposited. The deposit is divided into two blocks by a set of NNW-ESE-trending reverse faults, which uplifted the eastern block and exhumed thicker and deeper parts of the deposit. At least 200 m of volcano-sedimentary pile hosting the mineralization has been eroded in this block. By contrast, the western block exposes a shallower part of the system where cherts, amorphous silica and jasperoids occur. Three main stages of mineralization have been defined: (1) pre-ore stage is characterized by early quartz, pyrite and arsenopyrite, (2) base-metal and silver stage; characterized by sphalerite (6 to 15 mol% FeS), galena, chalcopyrite, pyrrhotite and Ag-bearing minerals (freibergite, polybasite, stephanite, pyrargyrite, freieslebenite and acanthite) and (3) post-ore stage; characterized by late quartz, kutnohorite and minor sulfides (arsenopyrite, sphalerite, pyrite, galena, Ag-bearing minerals and Pb-sulfosalts). Whole-ore geochemistry shows two groups of elements that are positively correlated; 1) Ag–Cd–Cu–Pb–Zn related to the base metal sulfides and 2) Au–As–Ge–Sb–W related to arsenopyrite and pyrite. Hydrothermal alteration is pervasive in the outcropping mineralized areas, including silicification and locally, vuggy silica textures. At depth, chloritic and sericitic alteration is developed along vein selvages and is superimposed to the regional propylitic alteration. Fluid inclusions indicate that the base-metal ores were deposited from 250 to 150 °C moderate salinity fluids (1–9 wt.% NaCl). The pre-ore stage is characterized by a saline fluid (6–22 wt.% NaCl) and between 210 and 250 °C whereas the post-ore stage has salinity of 4–8 wt.% and temperature from 175 to 215 °C. Cooling was the mechanism of ore mineral precipitation in the Patricia deposit, although mixing of fluids could have occurred in the pre-ore stage. Mineralogical, geochemical and fluid inclusion evidence is consistent with an intermediate sulfidation (IS) epithermal deposit type. This study highlights the high potential for hidden economic mineralization at depth in the western block and for extension of the ore body both to the south and to deeper levels in the eastern block of the Patricia ore deposit. To a larger extent, the implications of finding such polymetallic epithermal style of mineralization in the northern Chile Precordillera is relevant both to the regional metallogenic perspective and to the exploration potential of the region, where the late Eocene–early Oligocene metallogenic belt apparently disappears.

1. Introduction

Several long and linear, orogen-parallel metallogenic belts have been defined along the Chilean Andes, each one developed during a distinct metallogenic epoch, ranging from Cretaceous to Early Eocene times (Fig. 1a) (Camus and Dilles, 2001). The metallogenic belts young continentwards away from the subduction zone located at the Pacific western margin of South America, following a migration similar to the active magmatic arc systems with time (Coira et al., 1982). The Late Eocene to Oligocene belt is the most important because it hosts the largest concentration of Cu resources in the world, mostly in the form of world-class porphyry copper deposits such as Chuquicamata, La Escondida and El Salvador (Behn et al., 2001; Sillitoe and Perelló, 2005; Maksaev et al., 2007). These porphyry Cu deposits are genetically

* Corresponding author at: Departamento de Cristalografía y Mineralogía, Facultad de Ciencias Geológicas, Universidad Complutense de Madrid, C/ José Antonio Novais, s/n., 28040, Madrid, Spain.

http://dx.doi.org/10.1016/j.oregeorev.2015.10.026
0169-1368/

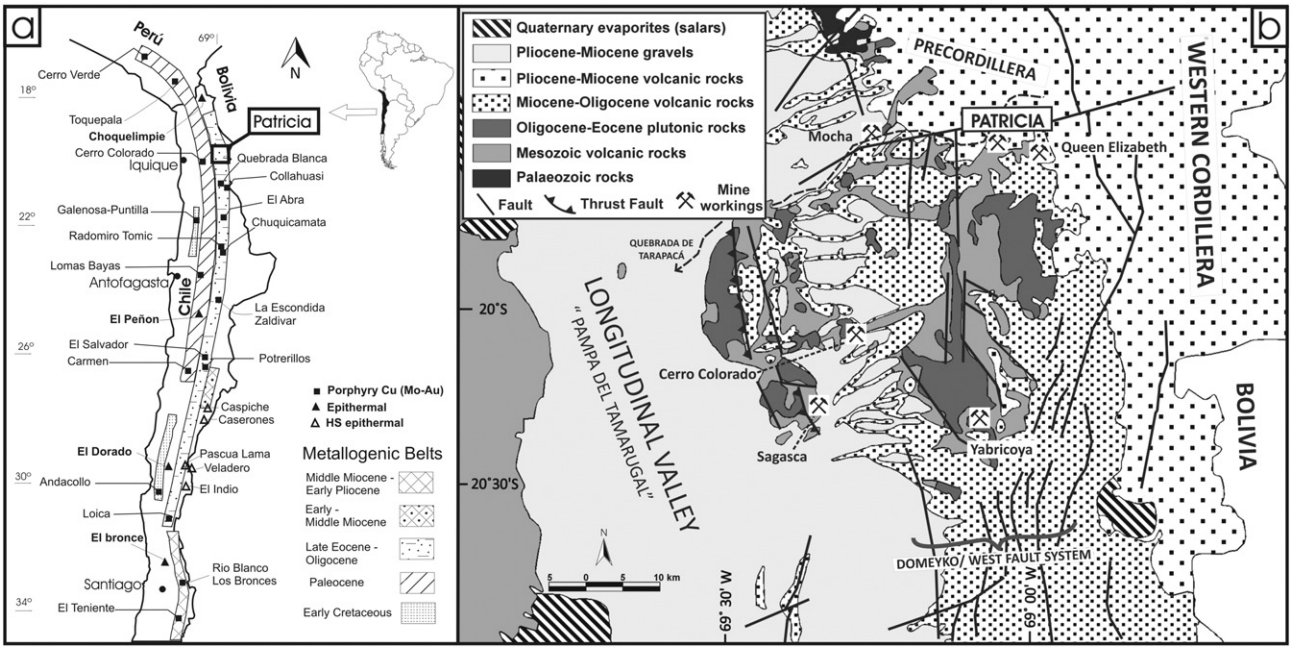

Fig. 1. (a) Location of the Patricia deposit and other Cenozoic deposits and prospects within major metallogenic belts of northern Chile and southern Peru (modified from Camus and Dilles (2001)) (b) Simplified regional geologic map of the Tarapacá region. The location of the Patricia deposit and nearby deposits and prospects in the area (Cerro Colorado, Sagasca, Yabricoya, Mocha and Queen Elizabeth) are shown.

related to epizonal plutons emplaced along the N-S oriented Domeyko fault system (Maksaev, 1990; Behn et al., 2001), whose episodic transpressional/transtensional kinematics eventually developed extensional areas favorable to the emplacement of shallow plutons. Queen Elizabeth deposit is the northernmost porphyry copper occurrence in the late Eocene–Oligocene belt within Chile (Sillitoe and Perelló, 2005). The apparent termination of the belt in this region is a result of concealment beneath Miocene volcanic rocks (Sillitoe, 2010), and it further reappears in southern Peru (Los Chancas, Cotabambas, Antapaccay, and Ataspaca porphyry-type deposits, among others; Sillitoe and Perelló, 2005).

The Patricia Zn–Pb–Ag ore deposit displays a vein-like geometry and intermediate sulfidation epithermal characteristics and it is located close to the northernmost end of the Late Eocene to Oligocene porphyry Cu belt in Chile, some kilometers apart from the Queen Elizabeth porphyry copper deposit (Fig. 1b). Geographically, it occurs in the Tarapacá Province, I Región, Chile, at latitude 19°81′S and longitude 69°06′W, 150 km northeast of Iquique and 30 km west of the international border with Bolivia (Fig. 1a and b). Other porphyry copper mines and prospects in the nearby region occur either related to the Paleocene–early Eocene belt (Cerro Colorado, Bouzari and Clark, 2002; Cotton, 2003; and Mocha, Sillitoe and Perelló, 2005) or to the late Eocene–early Oligocene belt (Yabricoya, Sillitoe, 1981; Sillitoe and Perelló, 2005) (Fig. 1b). The Patricia mineralization was identified in 2006 during the early stages of exploration carried out by Herencia Resources Plc over historical mine workings that date back to the nineteenth century. These historic workings focused on silver mining and consist of more than 1800 m of underground galleries; a 400 m long gallery intersected several major Zn–Pb–Ag mineralized veins. The Patricia ore deposit forms part of the Paguanta Mining Exploration Project and represents the only example known to date of economic Zn–Pb–Ag epithermal in the northernmost part of the Chilean late Eocene–Oligocene metallogenic belt, although other polymetallic epithermal deposits within the belt occur further south in the Antofagasta region (e.g. Faride, Camus and Skewes, 1991). The scarcity of this type of ore deposits in the Tarapacá region contrasts with the large number of examples known in the Peruvian and Bolivian Andes such as Caylloma and Pallancata in Peru (Echavarria et al., 2006; Gamarra-Urrunaga et al., 2013) and San Cristóbal in Bolivia (Phillipson and Romberger, 2004).

From a metallogenic point of view, the interest of the Patricia deposit is double. The polymetallic features of the Patricia mineralization, closer to those of the Peruvian and some Bolivian epithermal deposits than to the Chilean ones, may be indicating a change in the style of outcropping deposits and/or the level of erosion of the porphyry-epithermal systems in this area. On the other hand, the well-known genetic and spatial relationships between porphyry and epithermal deposits as parts of larger magmatic–hydrothermal ore systems (i.e. White and Hedenquist, 1995; Seedorff et al., 2005; Simmons et al., 2005; Sillitoe, 2010) highlight the potential of the region for finding hidden deposits in a sector of the Andean late Eocene–early Oligocene metallogenic belt apparently devoid of them.

In this contribution we describe a detailed study of the geology, mineralogy, geochemistry, and fluid inclusions at the Zn–Pb–Ag Patricia ore deposit. A major emphasis of the work has been to define the tectonic and structural framework of the deposit, and to identify and characterize the different stages of mineralization regarding both the mineralogy of the economic phases and the nature of the fluids responsible for ore deposition. The results allow us to address some key questions related to the evolution of the hydrothermal system, the mechanisms of ore deposition, and the potential of the area for discovery of new reserves in the future.

2. Regional context of the Paguanta Mining Exploration Project

The Paguanta Mining Exploration Project, led by Herencia Resources Plc, is located at an elevation of approximately 3600 m above sea level on the Quebrada of Tarapacá, a deep valley that runs through the Precordillera and the piedmont of the Andean Western Cordillera (Fig. 1b). In structural terms, the Precordillera is characterized in this area by the development of a west vergent fault system and associated folds (Pinto et al., 2004; Victor et al., 2004; Farías et al., 2005) corresponding to the southward continuation of the west vergent thrust system observed at the latitude of Arica. This major tectonic feature was likely associated with shortening and uplift of this part of the Andes

during the Cenozoic, Incaic and Quechua phases of the Andean cycle (see discussion by García and Hérail (2001) and Wörner and Seyfried (2001)). A thick sequence of clastic deposits and ignimbrites was also sourced in this part of the uplifting Precordillera during Oligocene and Miocene times (Schlunegger et al., 2010). These sediments unconformably overlie an early Palaeozoic to Palaeocene substratum.

At the regional scale, Mesozoic rocks are dominated by Cretaceous green–gray to black andesitic terrestrial sediments and subaerial lavas (Cerro Empexa and Cauquima Formation; Galli and Dingman, 1962; Sayes, 1978) which unconformably overlie Jurassic marine to subaerial sediments and volcanic sedimentary strata (Galli, 1957; Pacci et al., 1980; Tomlinson et al., 2001). These formations were intruded by Late Cretaceous to Paleogene granitoid stocks (Thomas, 1967; Galli, 1968) (Fig. 1b) and were deformed during the Incaic phase of the Andean orogenic cycle (Noble et al., 1979). Following this deformation event, an Oligo-Miocene succession consists of thick sequences of ignimbrites and gravels (Altos de Pica, Luja and Guaviña formations; Galli, 1957; Galli and Dingman, 1962; Pacci et al., 1980; Tomlinson et al., 2001). North-trending faults are the dominant structures (Fig. 1b), delimiting the horsts of the Sierra Juan de Morales and Sierra de Tarapacá (Galli, 1968) to the north of Yabricoya area. The Palaeozoic and Mesozoic basement has experienced continuous uplift between these faults since the initial Incaic Phase and subsequent Miocene uplift of the Altiplano. The area is incised by numerous west-southwest trending valleys (Fig. 1b), among which the Quebrada de Tarapacá (Bouzari and Clark, 2002) exposes the volcanic rocks hosting the Patricia ore deposit.

The Paguanta Mining Exploration Project includes a proven economic deposit (Patricia) and two prospects (La Rosa and Doris) in an area of around 40 km^2 (Fig. 2a). Patricia is an economic Zn–Pb–Ag vein-type mineralization containing mainly pyrite, sphalerite, galena and Ag-sulfosalts and hosted by hydrothermally altered andesitic rocks of uncertain age. Estimated mineral resources are 4.53 Mt., grading 3.7% Zn, 1.3% Pb, 83 g/t Ag and 0.2 g/t Au using a 2% Zn cut-off grade (June 2012, www.herenciaresources.com). The La Rosa prospect, located to the north of Patricia, consists of an intensely leached area with argillic alteration that extends to the Patricia area and is likely part of the same mineralizing system. The extension of the La Rosa prospect is well defined by a strong geophysical anomaly obtained through airborne gravimeters and covering more than 3 km^2. In spite of intense weathering, rocks have anomalously high contents of lead (0.41%), zinc (1.06%), copper (0.04%), gold (0.22 g/t) and silver (15.6 g/t). The Doris prospect is located north-northeast of Patricia and consists of a strongly altered zone with fractures filled with secondary copper minerals, mostly chrysocolla and malachite (Roel et al., 2013). Several sections of drill holes returned up to 2.5% Cu and 50 g/t Ag.

The country rocks in the Paguanta area are mostly volcanic and volcano-clastic in nature, probably correlative of the Cretaceous Cerro Empexa and Cauquima Formation (Galli and Dingman, 1962; Sayes, 1978). They exhibit a relatively complex structure of NW-SE-oriented asymmetrical folds. Detachment and fault-propagation types are present, the latter associated with steeply dipping sinistral thrust faults, which generally suppress a large part of the anticlinal short limbs. Folds and thrusts show vergence to both the SW and NE, suggesting the existence of flower structures at various scales. At the kilometer scale, the overall NW-SE orientation of folds and faults in the Paguanta area swings to more northerly orientations towards the north (Fig. 2a), suggesting it may represent the western part of a sinistral strike-slip duplex structure. This would be compatible with its location within the regionally important Domeyko fault system, a largely sinistral transpressional belt that has been active since ca. 35 Ma ago (Fig. 1b), a period during which 37 km of accumulated sinistral displacement has been estimated (Dilles et al., 1997; Tomlinson and Blanco, 1997a; Tomlinson and Blanco, 1997b; Maksaev and Zentilli, 1999; Campbell et al., 2006).

3. Analytical methods

In order to carry out mineralogical, geochemical and fluid inclusion studies, representative samples were selected from 206 exploration cores drilled by Herencia Resources Plc. and from surface exposures. Detailed logging of more than 200 m of 12 drill cores (8 in the eastern block and 4 in western block, see below) was performed to determine

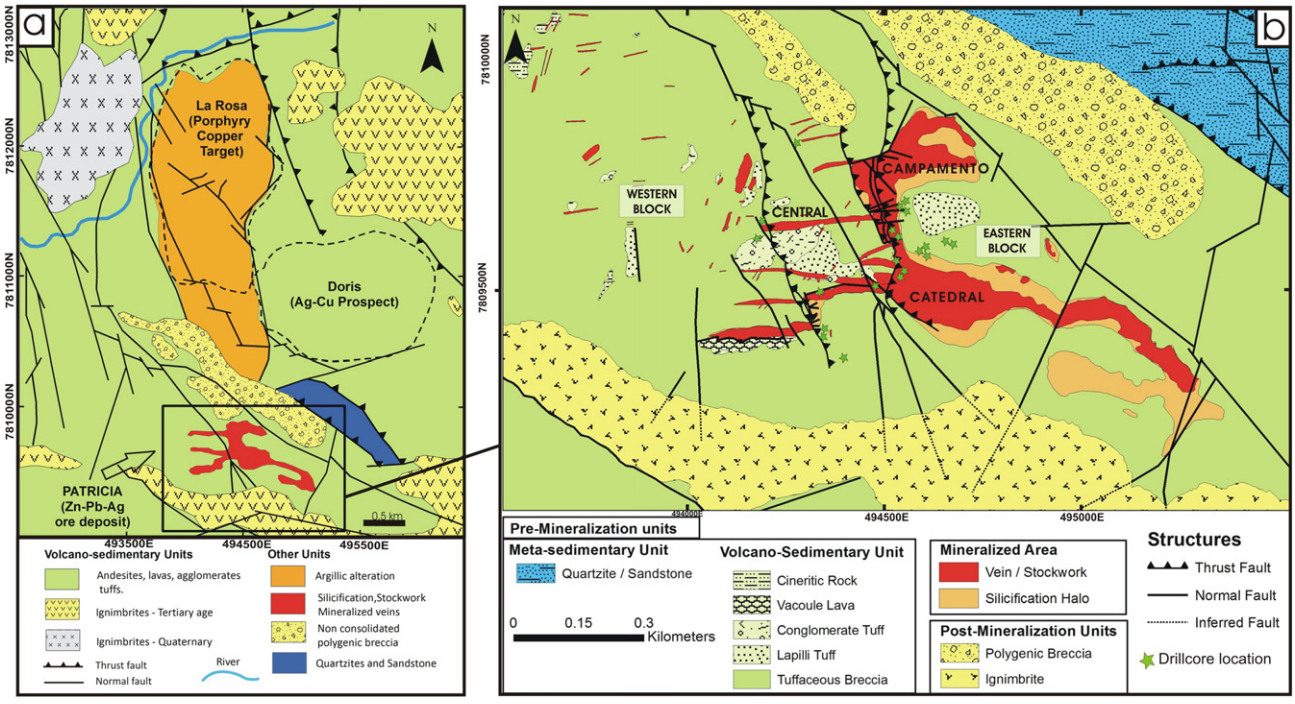

Fig. 2. (a) Simplified geological map showing the location of the three prospects (Patricia, Doris, La Rosa) within the Paguanta Mining Exploration Project (b) Geological map of the Patricia deposit showing the main units and the location of the three main mineralized veins (Campamento, Central and Catedral). Location of the drillcore sampling is also shown in the map. Drill cores are commonly N-S oriented and dip 40–60°S.

vein mineral relationships, textures and hydrothermal alteration patterns. A total of 221 polished thin sections were prepared and studied by transmitted and reflected light optical microscopy. Most of them correspond to the eastern block where the mineralization is better developed.

A semi-quantitative determination of the mineralogy of host rocks and mineralized veins was performed by X-ray diffraction (XRD) using a Siemens D500 XRD diffractometer with Cu Kα radiation and a graphite monochromator. The bulk mineralogy was studied in non-oriented powders and clay minerals in oriented aggregates prepared with the <2 μm fraction. The <2 μm clay fraction was sedimented from an aqueous suspension according to Stokes law (Moore and Reynolds, 1989). These oriented aggregates were air dried, treated with ethylene glycol and heated to 550 °C/2 h and then analyzed. Random powders were scanned from 2 to 65° and oriented aggregates were scanned from 2 to 30° 2θ with a scan speed of 0.02° 2θ/s.

The chemical compositions of ore minerals including base metal sulfides and Ag-bearing phases were determined by electron microprobe in 73 samples using a JEOL Superprobe JXA-8900 at the Centro Nacional de Microscopía Electrónica of the Universidad Complutense of Madrid, and a CAMECA Electron Microprobe Analyzer SX-50 at the Serveis Cientifico-tècnics of the Universitat of Barcelona. Kα X-ray lines were measured for: S, As, Fe, Co, Ni, Cu, Zn, Ag, Au, Cd, Sb, Te, Pb and Bi. The accelerating voltage was 20 kV; 50 nA beam current and 1–5 μm beam diameter. Counting times ranged from 20 to 60 s. The following standards were used: Galena, GaAs, Fe, NiCrCo, Cu, Zn, Ag, Au, Cd, GaSb, Te and Bi from the Smithsonian Institution and Harvard University (Jarosewich et al., 1980; McGuire et al., 1992).

Ten representative vein samples containing base metal sulfides and Ag-bearing phases were analyzed for whole-ore composition in Genalysis Laboratory Services Pty. Ltd., Maddington (Australia). Ag, As, Bi, Cd, Co, Mo, Se and Te contents were measured by inductively coupled plasma mass spectrometry (ICP-MS, multi-acid digest); Cu, Pb and Zn contents by inductively coupled plasma atomic emission spectrometry (ICP-OES, multi-acid digest); Au content by inductively coupled plasma mass spectrometry (ICP-MS, lead collection fire assay) and S content by infrared spectrometry. Linear regression and correlation between pairs of elements were computed using robust methods. These mathematical methods are appropriate for estimating correlation coefficients when samples are heterogeneous and the assumptions of normality and homoscedasticity required by classical statistical procedures cannot be guaranteed. Moreover, these methods are less influenced by anomalous data (outliers) than other classical methods. We computed correlation coefficients and p-value of the linear regression model with the lmrob function of the R package robustbase. The lmrob function uses fast MM-type estimators for linear regression models (Maronna et al., 2006).

Fluid inclusion chips were prepared from 13 core samples located between 94 m (lower limit of the superficial oxidized zone) and 230 m (lower depth reached by drilling) below present surface. The study of 108 fluid inclusions contained in 26 FIAs in these samples consisted of petrographic observations and microthermometric, laser ablation inductively coupled plasma mass-spectrometry (LA-ICP-MS) analyses and Raman spectroscopic analysis. Samples were selected in the Catedral vein drill cores as it is the largest and the best drilled vein in the deposit. This allowed a thorough sampling both at different depths (in order to check the occurrence of boiling) and along the vein strike. Besides the sample position in the deposit, the main criterion was selecting samples where quartz and/or sphalerite were well represented. This study was carried out in the Fluid Inclusions Laboratories of the Department of Crystallography and Mineralogy at the Complutense University of Madrid (Spain) and Virginia Tech in Blacksburg (USA). Fluid inclusion assemblages (FIAs) representing groups of inclusions that were trapped simultaneously (Bodnar, 2003; Goldstein and Reynolds, 1994) were identified based on detailed petrographic observations. Heating-freezing measurements were made on previously defined FIAs. Fluid inclusion homogenization and final ice melting temperatures were obtained using a Linkam heating-freezing stage (THMS600) mounted on an Olympus microscope. Salinity was calculated from final ice melting temperatures using the equation of Bodnar (1993) for the NaCl–H_2O system. The stage was calibrated using synthetic fluid inclusion standards (Sterner and Bodnar, 1984). The precision and accuracy of measured homogenization temperatures are estimated to be ± 1.0 °C and the precision and accuracy of ice-melting temperatures are estimated to be ± 0.1 °C.

The elemental concentrations of 46 individual fluid inclusions were measured using laser ablation-inductively coupled plasma-mass spectrometry (LA-ICP-MS). The LA-ICP-MS equipment consists of a 193 nm GeoLasPro Excimer Laser Ablation system coupled to an Agilent 7500ce inductively coupled plasma mass spectrometer. Fluid inclusions were ablated with a laser beam diameter selected such that the inclusion was wholly encompassed within the ablation pit. A NIST610 glass standard was analyzed before and after each sample for calibration and to correct for drift. For all inclusions, we analyzed for Au (dwell time: 50 ms), Ag (dwell time: 30 ms), Al, As, B, Ca, Cd, Cu, Fe, Ge, K, Mg, Na, Pb, Sb, Se, Si, Re, Te and Zn (dwell time: 10 ms). Data processing was carried out using the AMS software (Mutchler et al., 2008). Ag, As, Au, Cd, Cu, Re and Te concentrations were less than their detection limits in all analyzed samples with detection limits at 1 ppm. Qualitative element compositions of the host mineral were also indirectly obtained during ablation to intercept fluid inclusions.

Raman analyses were performed using a laser Raman micro-probe based on the Horiba LabRam-HR800 design with a high-resolution 800-mm spectrograph and equipped with an air-cooled 514-nm (green) argon laser set at 50 mW for excitation. The goal of the Raman analysis was to test for the presence of CO_2 and to identify clay minerals in fluid inclusions. Data management and analysis were performed using the statistical software R 3.1.2 (Team, 2014).

4. The Patricia Zn–Pb–Ag ore deposit

The Patricia ore deposit crops out in a small area of ~2 km^2 in which the following lithological units can be distinguished (Figs. 2b–3a):

1) Pre-mineralization units consist of: (1.1) a lower sedimentary succession which is represented by tightly folded and subvertical shales, sandstones and quartz-arenites, located NE of the Patricia mineralization and probably correlative to the Jurassic Noasa Formation elsewhere (Harambour, 1990); and (1.2) an upper volcano-sedimentary unit which hosts the Patricia mineralization and consists of a succession of subaerial, andesitic volcanic rocks, including breccias, pyroclasts, agglomerates, tuffs, lapilli and lavas, commonly affected by regional pervasive propylitic alteration. The volcano-sedimentary unit is folded and fractured along northwest-trending faults. The age of these rocks is uncertain, although a correlation with the Cretaceous Cerro Empexa and Cauquima Formations has been suggested (Galli and Dingman, 1962; Sayes, 1978).
2) Apart from slope debris, post-mineralization units are mainly represented by: (2.1) an ignimbrite sequence which unconformably overlies the folded volcano-sedimentary unit and the Patricia ore deposit at its southern end; and (2.2) a non-consolidated polygenic breccia that hosts variably-sized heterogeneous blocks of ignimbrite, andesite, quartzite, porphyritic rocks, hematite ore and granitoids.

Four main E-W- to ENE-WSW-oriented mineralized vein systems are recognized in the area, named from north to south, Campamento, Central, Catedral (Figs. 2b–3a) and Carlos. These vein systems are better developed in the eastern part of the deposit (Fig. 2b) and they range in thickness from 1 to 100 m in the Catedral vein and from 1 to 15 m in the Campamento, Central and Carlos veins. The vein length at surface varies from 400 m for the Central vein to around 600 m for the Catedral and Campamento veins, whereas the Carlos vein does not crop out and is

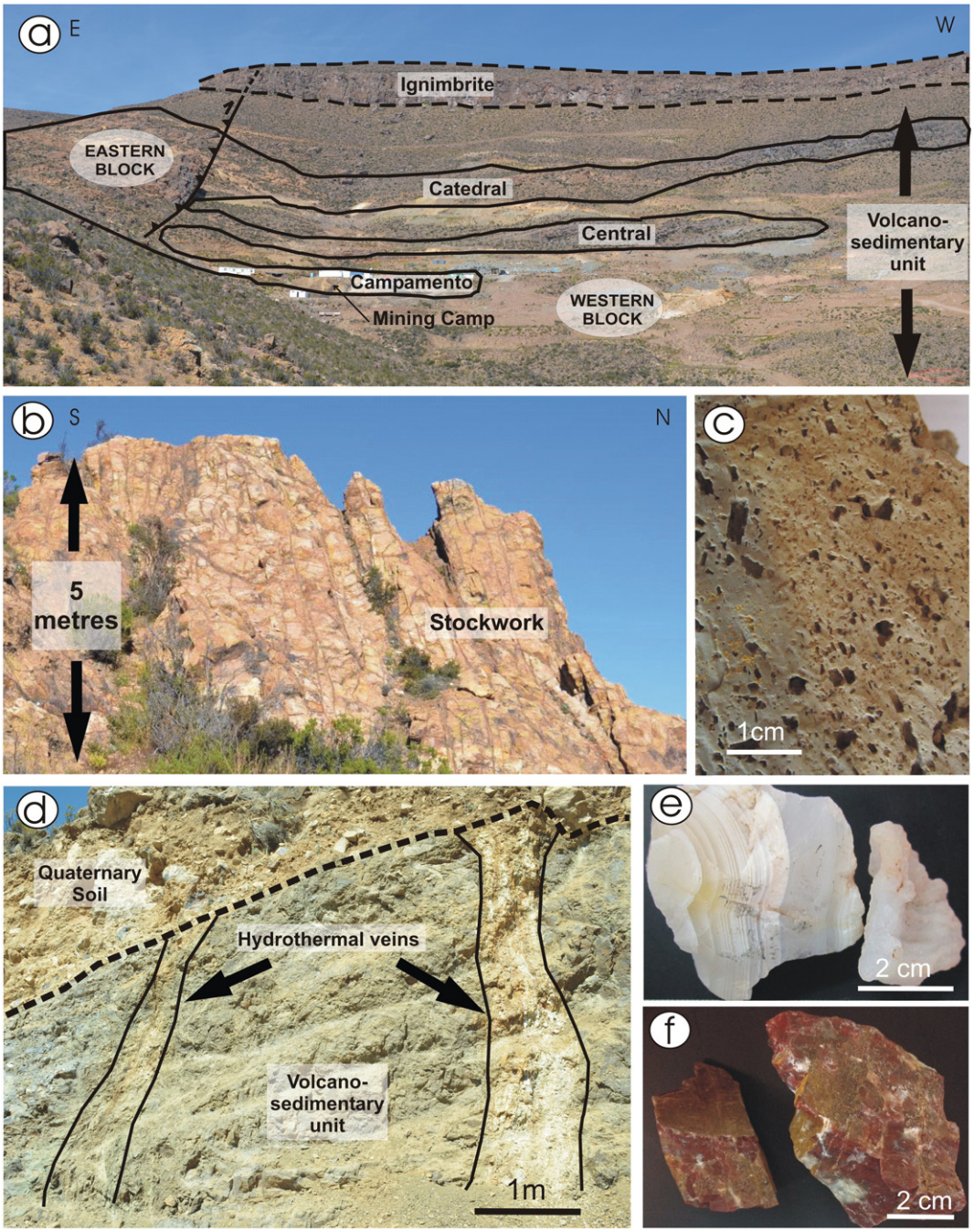

Fig. 3. (a) General view of the western block in the Patricia ore deposit with the mineralized units within the volcano-sedimentary unit represented in solid lines and the post-mineralization unit represented by dashed lines. The main thrust fault system and the position of the western and eastern blocks are also shown, (b) overview of the Patricia silicification and stockwork area in the eastern block, (c) detailed photograph of the vuggy silica texture observed at Patricia ore deposit, (d) general geometry of the hydrothermal vein system in the western block, (e–f) sample of amorphous silica and jasperoids, respectively, located in the Patricia western block.

only observed in drill cores. The vein systems generally thin out towards both the east and west from a thicker central zone where the historical and present mine workings are concentrated. Internally, these vein systems consist of stockworks with veinlets from 1 to 10 cm wide, striking NW-SE, NE-SW and E-W, and mostly showing steep inclinations although some gently dipping veinlets are also locally recognized. E-W veinlets are thicker than other veinlets in the stockwork and this is consistent with the E-W orientation of the four major mineralized veins. These structural features of the mineralization within the dominant northwest-trending fault system (Fig. 2b) indicate that the Patricia ore deposit was emplaced under a sinistral strike-slip regime, probably as a part of an extensional (transtensional) duplex.

At the deposit scale, the area is transected by a prominent tectonic structure represented by a set of parallel NNW-SSE thrust faults that post-date the mineralization, the most important of which is partly exposed along an overhanging cliff close to the mining camp (Figs. 2b–3a). Kinematic indicators show reverse fault movement. However, a mineralized stockwork area connects the Campamento and Catedral veins along these faults in the central part of the deposit (Fig. 2b), thus suggesting that these NNW-SSE structures were already active during the mineralization event, although not necessarily as thrust faults. The thrust set structure divides the area into different blocks, with the eastern blocks always in the hanging-wall. The easternmost block has steep relief and is characterized by a well-developed silicified lithocap with

intense oxidized-vein stockwork and locally vuggy silica textures at the surface (Fig. 3b–c). Unmineralized silicification halos typically surround the outcropping mineralized veins (Fig. 2b) and extend to ~30 m below the surface, according to drill core observations. The western blocks commonly show less steep slopes and are characterized by an intense weathering and argillic alteration associated with oxidized vein systems at the surface (Fig. 3d). Mineralized veins are here thinner and poorer in their metal contents, although silicification and stockwork structures are also present but to a lesser extent. The occurrence of chert, amorphous silica, jasperoids and calcite in or close to the surface is also common in the westernmost part of the deposit (Fig. 3e–f).

The host rocks are affected by locally intense hydrothermal alteration close to the mineralized veins. This alteration is superimposed on the earlier regional propylitic alteration (Fig. 4a). As a consequence, primary textures are poorly preserved. Hydrothermal alteration includes chloritization (chlorite ± pyrite ± arsenopyrite ± apatite ± rutile, Fig. 4b) and sericitization (quartz + sericite/illite ± pyrite ± kutnohorite, Fig. 4c). The chloritic alteration gives rise to a distinctive pale-green color that is pervasive and results in complete transformation of mafic minerals and plagioclase to chlorite (chamosite and clinochlore) along with minor formation of pyrite, arsenopyrite, apatite and rutile. Pyrite and arsenopyrite occur as disseminations of euhedral to subhedral crystals (0.5–3 mm) throughout the host volcanic rock (Fig. 4b). The sericitic alteration surrounds and partially overprints the chloritic alteration (Fig. 4c). Chlorite and illite also occur within the veins in contact with ore minerals.

5. Mineralogy of the ore deposit

5.1. Mineral assemblages and paragenetic sequence

Ore minerals in the Patricia ore deposit consist, in decreasing order of abundance, of: pyrite, sphalerite, galena and arsenopyrite, minor amounts of chalcopyrite, pyrrhotite and Ag-bearing minerals (freibergite, polybasite, stephanite, pyrargyrite, freieslebenite and acanthite) and trace amounts of boulangerite ($Pb_5Sb_4S_{11}$) and jamesonite ($Pb_4FeSb_6S_{14}$). Representative chemical compositions of sulfide phases and Ag-bearing minerals are given in Tables 1 and 2. Based on ore mineralogy and textures, several distinct veins have been identified (Fig. 5): (a) symmetric mineralized veins composed mainly of pyrite ± arsenopyrite on the edges, quartz in the outer bands and sulfides, with chlorite ± kutnohorite in the center (Fig. 5a); (b) asymmetric veins with sphalerite, arsenopyrite and quartz (Fig. 5b); (c) brecciated sulfides cemented by quartz and arsenopyrite (Fig. 5c); (d) veinlets (from 0.1 to 5 cm) of pyrite and sphalerite (Fig. 5d); (e) massive veins of sulfides (Fig. 5e); and (f) veinlets (from 0.5 to 3 cm) composed of quartz and pyrite ± arsenopyrite (Fig. 5f). Based on the different vein types and the textural relationships between them, three mineralization stages (pre, main, and post-ore stages) have been established (Fig. 6).

5.1.1. Stage 1: Pre-ore stage

The stage 1, or pre-ore stage, is characterized by the deposition of quartz (Qz1), pyrite (Py1) and minor arsenopyrite (Apy1) in veins that may be later filled by sphalerite and galena during the main stage of mineralization (Figs. 5a and 7a), suggesting a successive re-opening of veins. At the contact with the host rock, Qz1 occurs as fine-grained crystals (<0.5 mm) that grow to elongated and larger crystals (>2 mm) towards the vein center, developing comb textures typical of open-space filling (Fig. 7b). Py1, the main sulfide of the stage 1, occurs as euhedral to subhedral crystals (0.5–1.5 mm) distributed mainly along the boundaries of the veins (Figs. 7a and c) and also as individual euhedral grains in the central part of the veins filled with Qz1 (Fig. 5f). Py1 is typically zoned with As-rich bands (up to 1.5 at.% As) (Fig. 7d). In these zoned grains, S is negatively correlated with As and Sb whereas As is positively correlated with Sb. Py1 is selectively replaced by sphalerite and galena of the main stage (Fig. 7e). Apy1 occurs as euhedral to subhedral grains (0.5–1 mm) in close spatial relationship with Py1 and

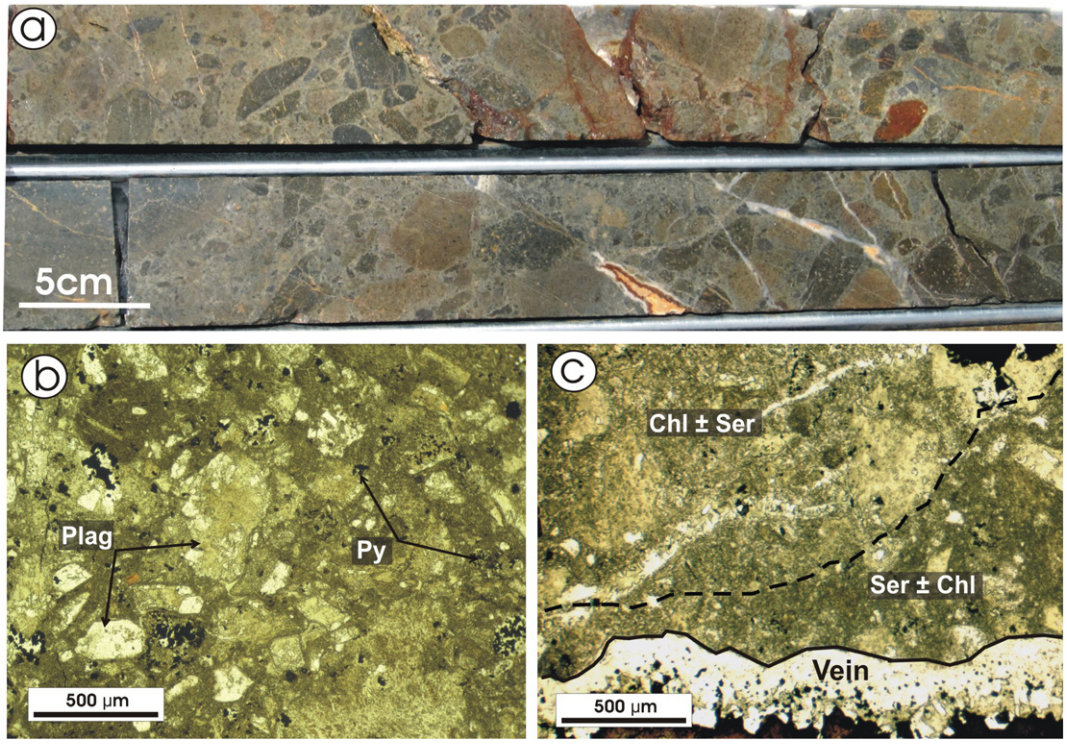

Fig. 4. (a) Drill core section showing the volcanic and volcano-clastic andesitic breccias hosting the mineralization and regionally affected by chloritic alteration. Photomicrographs in transmitted light with one polarizer of: (b) the typical altered host rock in the Patricia deposit affected by chloritic alteration (greenish to brownish colors). Relicts of plagioclase and disseminate of pyrite are also visible and (c) vein showing sericitic (illite) alteration selvage overprinting the chloritic alteration of the host rock. Abbreviations: *Py* = Pyrite, *Plag* = Plagioclase, *Chl* = Chlorite, *Ser* = Sericite.

Table 1
Representative EPMA analyses of the sulfides minerals in the Patricia ore deposit from each stage of mineralization. n = Number of electron microprobe analyses of each mineral. LOD = limit of detection of the Electron Microprobe for each element in wt.%. Abbreviations: Py_1 = Pyrite stage 1, Apy_1 = Arsenopyrite stage 1, Sp_{2A} = Sphalerite stage 2A, Sp_{2B} = Sphalerite stage 2B, Gn_{2B} = Galena stage 2B, Py_3 = Pyrite stage 3, Sp_3 = Sphalerite stage 3, Gn_3 = Galena stage 3, Apy_3 = Arsenopyrite stage 3. *b.d = below detection limit.

Stage	Stage 1 (pre-ore stage)				Stage 2 (Base-metal and silver stage)						Stage 3 (post-ore stage)					LOD
Substage					Substage 2-A	Substage 2-B										
Mineral	Py_1	As-rich Py_1	Apy_1	Sb-rich Apy_1	Sp_{2A}	Sp_{2B}	Gn_{2B}	Chalcopyrite	Pyrrothite	Py_3	As-rich Py_3	Sp_3	Gn_3	Apy_3	Sb-rich Apy_3	
#	215	145	170	162	132	172	136	29	4	37	14	23	17	209	205	
As (wt%)	0.83	2.70	42.96	45.86	b.d	b.d	b.d	b.d	b.d	0.12	1.85	b.d	b.d	42.77	41.04	0.05
Ag	b.d	b.d	b.d	b.d	b.d	b.d	0.08	b.d	b.d	0.02	b.d	b.d	0.03	0.03	b.d	0.02
Au	0.03	b.d	0.07	0.03	b.d	b.d	b.d	b.d	b.d	b.d	b.d	b.d	b.d	b.d	0.05	0.03
Fe	46.23	45.25	35.21	34.06	6.56	8.44	0.12	29.22	59.17	46.49	45.86	5.90	0.14	35.69	35.77	0.02
Zn	0.07	b.d	b.d	b.d	58.90	56.53	b.d	0.87	1.78	0.40	0.05	59.69	0.09	b.d	0.03	0.03
Co	0.05	0.05	0.04	0.05	b.d	0.02	b.d	0.03	0.06	0.02	0.07	b.d	b.d	0.06	0.03	0.02
Cd	b.d	b.d	0.03	b.d	0.27	0.30	0.10	b.d	b.d	0.04	0.06	0.22	0.07	b.d	b.d	0.02
S	53.05	52.13	21.01	18.10	34.05	33.89	13.07	35.65	39.21	52.93	52.13	33.74	13.23	22.03	20.62	0.05
Cu	b.d	b.d	b.d	b.d	b.d	b.d	b.d	34.36	0.03	b.d	0.07	b.d	0.58	b.d	b.d	0.03
Pb	0.26	0.25	0.11	0.13	0.14	0.15	87.12	0.18	0.22	0.20	0.15	0.14	85.28	0.09	0.08	0.03
Sb	0.03	0.02	0.22	2.45	0.07	0.09	0.32	0.02	0.05	b.d	0.05	0.02	0.16	0.25	3.14	0.02
Total	100.55	100.39	99.64	100.68	99.99	99.43	100.80	100.32	100.51	100.22	100.29	99.70	99.57	100.92	100.77	
As (apfu)	0.01	0.04	0.92	1.02	–	–	–	–	–	–	0.03	–	–	0.90	0.88	
Ag	–	–	–	–	–	–	–	–	–	–	–	–	–	–	–	
Au	–	–	–	–	–	–	–	–	–	–	–	–	–	–	–	
Fe	0.99	0.98	1.02	1.01	0.11	0.15	0.01	0.96	0.92	1.00	0.99	0.10	0.01	1.01	1.03	
Zn	–	–	–	–	0.86	0.83	–	0.02	0.02	0.01	–	0.88	–	–	–	
Co	–	–	–	–	–	–	–	–	–	–	–	–	–	–	–	
Cd	–	–	–	–	–	–	–	–	–	–	–	–	–	–	–	
S	1.99	1.97	1.06	0.94	1.02	1.02	0.98	2.03	1.06	1.99	1.97	1.01	0.98	1.08	1.04	
Cu	–	–	–	–	–	–	–	0.99	–	–	–	–	0.02	–	–	
Pb	–	–	–	–	–	–	1.01	–	–	–	–	–	0.98	–	–	
Sb	–	–	–	0.03	–	–	0.01	–	–	–	–	–	–	–	0.04	
Total	3.00	3.00	2.99	3.00	2.00	2.00	1.99	4.00	2.00	3.00	2.99	2.00	1.99	2.99	3.00	

usually shows zoned crystals with Sb-rich bands (up to 5.2 at.% Sb) (Fig. 7f). The As content in Apy1 ranges from 26.9 to 33.9 at.%. The Sb content is positively correlated with As and negatively correlated with S.

5.1.2. Stage 2: Base-metal and Ag stage

The stage 2, or base-metal and Ag stage, represents the highest volume of mineralization in the Patricia ore deposit. During this stage, base metal sulfides and Ag-bearing minerals precipitated in symmetric (Fig. 5a), asymmetric (Fig. 5b) and massive veins (Fig. 5e). This stage can be divided into two substages (Fig. 6): substage 2A is characterized by sphalerite (Sp2A) and minor amounts of chalcopyrite and pyrrhotite, while substage 2B is characterized by abundant brecciation (Fig. 5c) and the precipitation of sphalerite (Sp2B) and galena (Gn2B) and minor chalcopyrite, pyrrhotite and Ag-bearing phases, including freibergite, pyrargyrite, polybasite, stephanite, freieslebenite and acanthite. Minor quartz and pyrite are occasionally observed in this stage. Sp2A occurs as massive aggregates (0.5 to >2 mm) of zoned crystals, locally forming banded sphalerite (Fig. 8a–b). Zn and Fe contents of Sp2A range from 37.9 to 45.9 at.% and from 3.2 to 10.9 at.% (6.4–17.6 mol% FeS), respectively. Sp2B also occurs as coarse to fine-grained aggregates (<0.5 to >2 mm) of zoned crystals. In contrast to Sp2A, Sp2B hosts numerous blebs of chalcopyrite ("chalcopyrite disease") and pyrrhotite and is in close spatial relationship to galena (Gn2B) and Ag-bearing minerals (Fig. 8c–d). Sp2B has contents of Zn and Fe similar to Sp2A (39.3–44.8 at.% Zn and 4.2–9.4 at.% Fe) with Fe ranging from 7.7 to 15.5 mol%. The Cd content in both types of sphalerite is typically less than 0.2 at.% and does not show any correlation with Zn. Gn2B usually fills voids within Sp2B grains (Fig. 8d–e). The Pb content ranges from 47.9 to 51.7 at.% and Ag content is invariably below the detection limit of the EPMA. Gn2B contains significant amounts of Sb, usually higher than 0.2 at.% and up to 0.67 at.%, but no significant correlation between Sb and Pb contents is observed. Chalcopyrite and pyrrhotite mainly occur as inclusions or blebs (<50 μm) within Sp2B (Fig. 8c–d), and also as individual grains (10–100 μm) filling voids between Sp2B and Gn2B in close spatial relationship with Ag-bearing minerals. Pyrrhotite is Fe-poor with an average Fe content of 46.1 at.%. Furthermore, Fe-rich chlorite and illite occur in close association with sphalerite and galena within mineralized veins (Fig. 8f). Fe-rich chlorite is more abundant than illite that occurs as small crystals intergrown with Fe-rich chlorite. These chlorites are systematically of chamositic type with Fe content up to 46.4 at.%. The presence of chlorite and illite may provide useful information about the pH of fluids (e.g. Romberger, 1991; Moncada and Bodnar, 2012) and the existence of different mineralizing fluids.

5.1.3. Stage 3: Post-ore stage

The stage 3, or post-ore stage, is characterized by: (a) the formation of quartz (Qz3) and arsenopyrite (Apy3) cementing brecciated sulfides of the second stage (Figs. 5c–9a); (b) small veinlets (0.2–5 cm) of pyrite (Py3) and sphalerite (Sp3) forming local stockwork (Fig. 5d) and (c) the late formation of kutnohorite. During the post-ore stage, minor galena (Gn3), Ag-bearing phases (freibergite, pyrargyrite, freieslebenite and acanthite) and Pb sulfosalts (boulangerite and jamesonite) have also precipitated. In the contact with brecciated sulfides, Qz3 occurs as microcrystalline crystals (<0.2 mm) whereas outwards it forms large mosaic-textured crystals (from 0.5 to >5 mm) (Fig. 9b) and small geodes indicating open-space filling. Apy3 forms subhedral zoned grains with Sb-rich bands in close association with Qz3 (Fig. 9c–d). In contrast to Apy1, the As content of Apy3 shows a narrow range (29.5–30.7 at.%) and the Sb content of the Sb-rich bands is lower (up to 1.4 at.%). Sb content is positively correlated with As and negatively correlated with S. Py3 occurs as euhedral to anhedral crystals (0.2–1 mm) and usually contains As-rich bands (up to 1 at.%). In these As-rich bands, S is also negatively correlated with As and Sb, and As is positively correlated with Sb as in Py1. Sp3 is similar to Sp1 and Sp2 and also occurs as massive aggregates of zoned crystals (Fig. 9e–f). Zn and Fe contents of Sp3 are also similar to those of Sp1 and Sp2, ranging from 40.8 to 44.9 at.% and from 3.9 to 7.8 at.%, respectively (7.5–13.2 mol% FeS). The Cd

Table 2
Representative EPMA analyses of the Ag-bearing minerals present in the Patricia ore deposit. LOD = limit of detection in wt.%. *b.d = below detection limit. Abbreviations. *Py* = Pyrite, *Sp* = Sphalerite, *Gn* = Galena, *Ccp* = Chalcopyrite.

Sample	Freibergite			Polybasite			Pyrargyrite		Stephanite		Freieslebenite		Acanthite		LOD
Label	PT52.205.46	PT 52-205.84	PT-41 193.00	PT-52-188,19	PT-52-188,19	PT-52-209,93	PT52-205,62	PT41 - 193,00	PT52-208,82	PT-52-209,95	PT35-68.45	PT41-192,92	PT-41 193.25	PT52-203,52	
Analysis #	15	137	196	52	53	77	94	275	62	98	105	183	230	60	
As (wt %)	0.11	0.08	0.06	0.11	b.d	0.31	0.13	b.d	0.32	b.d	b.d	b.d	0.06	0.23	0.05
Ag	21.86	33.28	28.28	67.78	67.80	68.24	60.52	60.66	72.69	75.19	21.90	24.16	82.16	87.26	0.02
Au	b.d	b.d	b.d	b.d	b.d	b.d	b.d	b.d	b.d	b.d	b.d	b.d	b.d	b.d	0.03
Fe	5.33	4.50	5.34	0.68	3.24	0.30	0.34	0.05	0.26	0.04	0.44	0.03	0.31	0.04	0.02
Zn	1.08	1.76	0.68	0.38	0.03	0.16	0.09	b.d	1.64	0.03	b.d	0.10	0.08	0.03	0.03
Cd	b.d	0.27	0.39	b.d	b.d	b.d	b.d	b.d	b.d	b.d	b.d	0.34	1.22	b.d	0.02
S	22.01	20.30	21.05	13.93	16.25	15.35	16.84	17.09	13.74	14.48	19.71	18.61	15.47	10.04	0.05
Cu	22.72	13.49	15.86	4.12	4.42	3.37	0.12	0.06	2.81	2.04	b.d	b.d	0.22	0.04	0.03
Pb	0.15	0.11	1.89	b.d	b.d	b.d	0.19	0.96	0.35	0.24	30.93	31.06	0.38	2.21	0.03
Sb	27.73	25.93	27.18	13.31	9.14	11.36	22.54	22.81	8.97	8.42	27.93	26.55	0.10	b.d	0.02
Total	100.98	99.73	100.73	100.31	100.92	99.09	100.77	101.66	100.78	100.44	100.92	100.85	100.01	99.85	
As (apfu)	0.03	0.02	0.01	0.03	0.01	b.d	0.01	–	0.03	–	–	–	–	0.01	
Ag	3.70	6.05	5.03	14.50	13.61	14.45	3.06	3.05	5.37	5.57	1.01	1.14	1.80	2.13	
Au	–	–	–	–	–	–	–	–	–	–	–	–	–	–	
Fe	1.74	1.58	1.84	0.28	1.26	0.12	0.03	–	0.04	0.01	0.04	–	0.01	–	
Zn	0.30	0.53	0.20	0.13	0.01	0.06	0.01	–	0.20	–	–	0.01	–	–	
Cd	–	0.05	0.07	–	–	–	–	–	–	–	–	0.02	0.03	–	
S	12.53	12.42	12.60	10.03	10.98	10.94	2.86	2.89	3.41	3.61	3.06	2.96	1.14	0.83	
Cu	6.53	4.16	4.79	1.50	1.51	1.21	0.01	0.01	0.35	0.26	–	–	0.01	–	
Pb	0.01	0.01	0.18	–	–	–	0.01	0.03	0.01	0.01	0.74	0.76	–	0.03	
Sb	4.16	4.18	4.28	2.52	1.63	2.13	1.01	1.02	0.59	0.55	1.14	1.11	–	–	
Total	29.00	29.00	29.00	29.00	29.00	28.91	7.00	6.99	10.00	10.00	6.00	6.00	2.99	3.00	
Size Ø	250 μ	40 μ	100 μ	90 μ	20 μ	45 μ	15 μ	20 μ	65 μ	145 μ	10 μ	15 μ	15 μ	12 μ	
Host mineral	Py/Gn/Ccp	Sp/Gn	Sp	Gn	Sp/Gn	Sp/Gn	Gn	Gn	Sp/Gn	Gn	Gn	Gn	Gn	Gn	

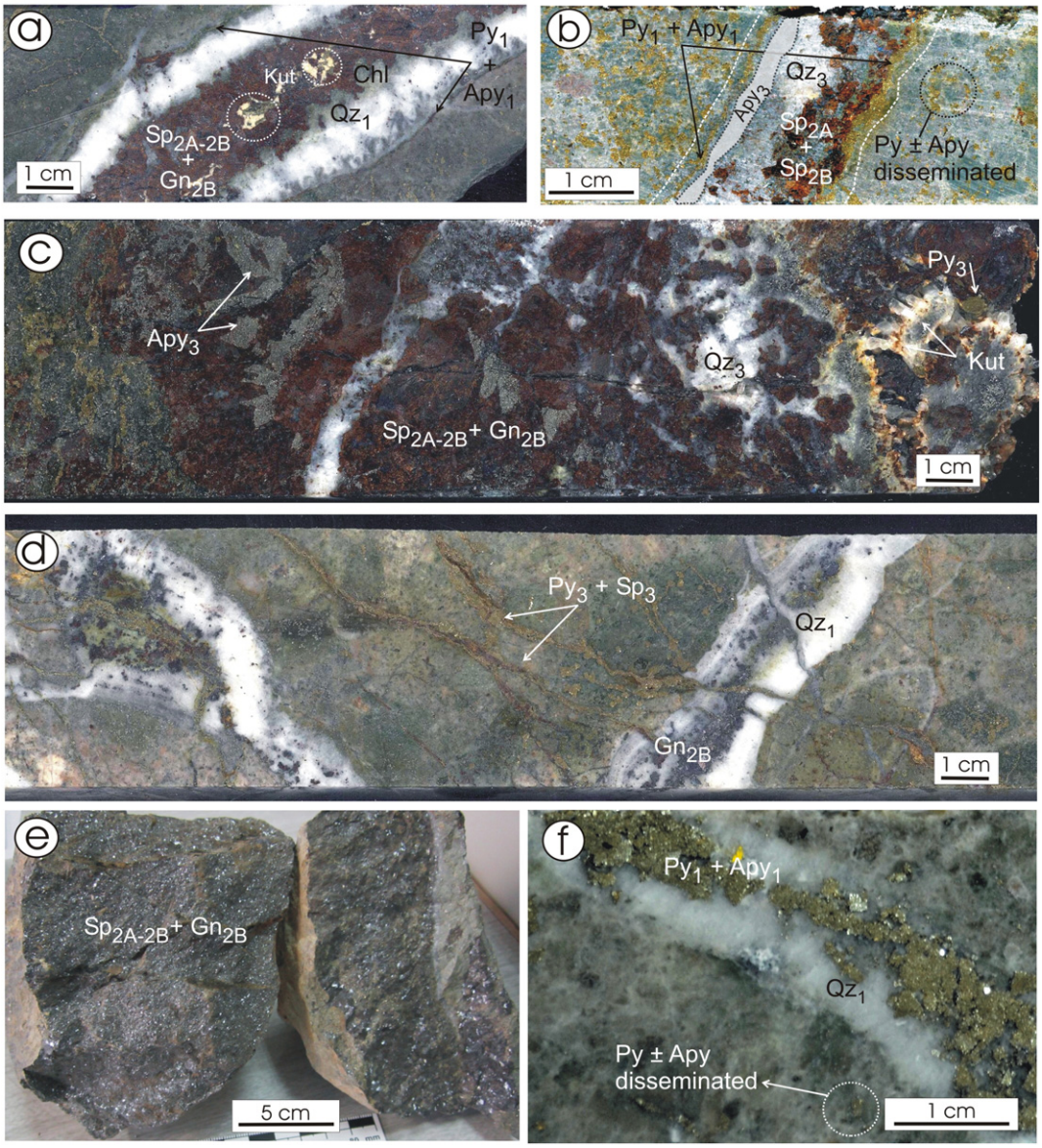

Fig. 5. Drill-core sections showing the different types of mineralized veins observed in the Patricia ore deposit; (a) symmetric, (b) asymmetric, (c) brecciated sulfides cemented by Qz_3 and Apy_3, (d) veinlets of pyrite and sphalerite, (e) massive sulfide and (f) veinlets mainly composed of quartz and pyrite ± arsenopyrite. Abbreviations: *Py_1* = Pyrite stage 1, *Apy_1* = Arsenopyrite stage 1, *Sp_{2A}* = Sphalerite stage 2A, *Sp_{2B}* = Sphalerite stage 2B, *Gn_{2B}* = Galena stage 2B, *Py_3* = Pyrite stage 3, *Sp_3* = Sphalerite stage 3, *Gn_3* = Galena stage 3, *Apy_3* = Arsenopyrite stage 3, *Qz_1* = Quartz stage 1, *Qz_3* = Quartz stage 2 and *Kut* = Kutnohorite.

content of Sp3 is less than 0.13 at.% and does not correlate with Zn. Gn3 occurs as minor aggregates and shows a narrow range in Pb content (46.3–48.6 at.%) and contains significant amounts of Sb (average 0.4 at.% and up to 1.9 at.%). The Ag content, in most analyzed Gn3 grains, is below the detection limit of the EPMA. Freieslebenite, boulangerite and jamesonite, with grain sizes ranging from 5 to 25 μm, occur in close relationship with Ag-bearing minerals and filling voids within Gn3 (Fig. 9h). Kutnohorite, interpreted as the last mineral that precipitated in the paragenetic sequence, occurs as euhedral and subeuhedral grains forming narrow veins that cross-cut the brecciated sulfides of the second stage (Fig. 9g).

5.2. Mineralogy and chemistry of Ag-bearing minerals

A total of 230 grains of Ag-bearing phases were identified and analyzed in 30 polished thin sections. Ag-bearing minerals are present in substage 2B in close textural relationship to galena (more than 80% of the Ag-bearing minerals are located within galena), sphalerite and chalcopyrite and also in the post-ore stage in close relationship to kutnohorite and minor sulfides. The Ag-bearing minerals identified are, in decreasing order of abundance, freibergite, polybasite, stephanite, pyrargyrite, freieslebenite and acanthite. They regularly occur as anhedral grains ranging in size from less than 10 μm up to 200 μm, but average around 40 μm and usually are located at the boundaries of galena and sphalerite or close to the contact with sphalerite, chalcopyrite and pyrite (Fig. 10). Representative analyses of different Ag-bearing phases are reported in Table 2.

5.2.1. Freibergite

$(Ag, Cu)_{10}(Fe, Zn)_2Sb_4S_{13}$ represents 90% of the total Ag phases identified. It occurs as anhedral grains (15–500 μm but commonly <60 μm) located at the boundaries of Gn_{2B} and Sp_{2B} grains and close to the contact with pyrite, chalcopyrite, silicates and kutnohorite (Fig. 10a–b). The Fe and Zn content in individual grains of freibergite is homogeneous and has an Fe content systematically higher than Zn. Ag ranges from 11 to 21.7 at.% with an average of 15.1 at.%, and Cu ranges from 13.3 to

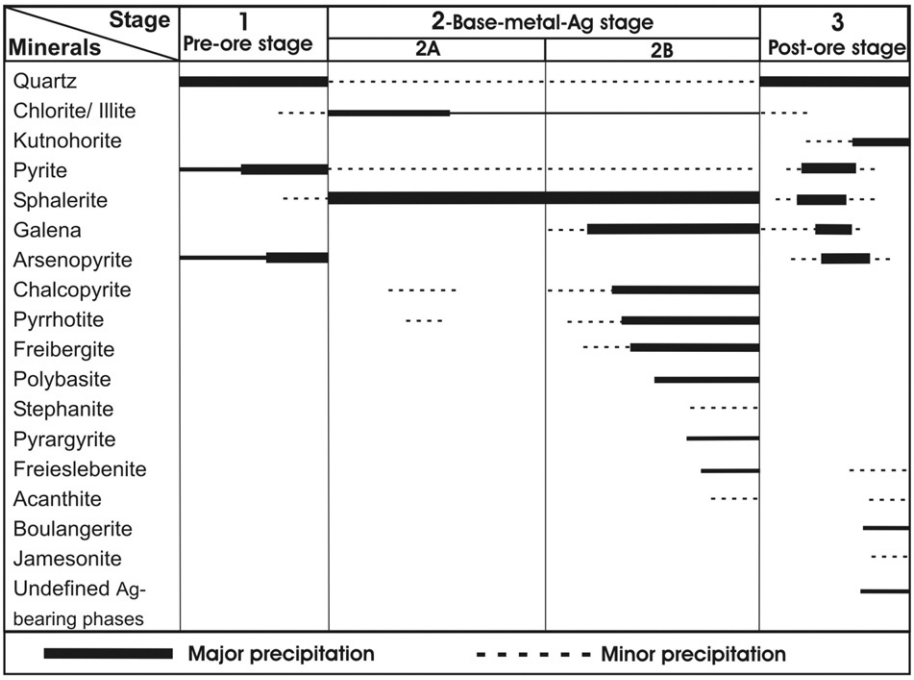

Fig. 6. Mineral assemblages and paragenetic sequence present in the Patricia ore deposit. Thick bars indicate higher abundances, thin and dashed lines refer to lower abundances.

23.9 at.% with an average of 19.4 at.%. Arsenic content is invariably below 0.2 at.%.

5.2.2. Polybasite

$(Ag, Cu)_{16}(Sb, As)_2S_{11}$ typically forms fine-grained crystals (10–60 μm) intergrowth with freibergite (Fig. 10a) or elongated grains along cleavage planes within Gn_{2B} crystals (Fig. 10c). Unlike freibergite, polybasite is invariably contained within galena and has not been observed within sphalerite. Electron microprobe analyses reveal that Ag content ranges from 46.9 to 49.8 at.% with minor substitution by Cu (up to 1.5 apfu). Sb content ranges from 5.6 to 8.7 at.% and As content is below 0.3 at.%.

5.2.3. Pyrargyrite

(Ag_3SbS_3) occurs as anhedral grains (5–40 μm) disseminated within Gn_{2B}, Gn_3 and commonly in close relationship with kutnohorite (Fig. 10d). It is particularly common in samples with high modal abundance of Ag-bearing minerals. Its composition is almost stoichiometric with Ag content around 43.7 at.%.

5.2.4. Stephanite

(Ag_5SbS_4) is a very minor Ag-rich sulfosalt in the Patricia ore deposit and commonly coexists with polybasite and freibergite with grain sizes of up to 30 μm. It contains 53.7–55.7 at.% Ag and up to 3 at.% Cu.

5.2.5. Freieslebenite

($AgPbSbS_3$) forms small-elongated 30 to 200 μm grains within galena (Fig. 10e), and it is also in close relationship to other Pb sulfosalts such as boulangerite and jamesonite. Ag and Pb contents range from 16.9 to 19 at.% and from 12.4 to 12.7 at.%, respectively.

5.2.6. Acanthite

(Ag_2S) represents the most Ag-rich mineral (from 60 to 71.1 at.%) found in the Patricia ore deposit. However, it is a very minor phase and usually occurs as anhedral 5 to 10 μm grains, closely related to freibergite and pyrargyrite (Fig. 10f). It is also observed at the boundaries between sphalerite and galena or in close relationship to kutnohorite.

6. Whole-ore composition of the mineralized veins

Results of multi-element analyses for selected ore samples are given in Table 3. Matrices of statistically significant correlations and scatterplots for pairs of elements in whole-ore samples are given in Fig. 11. According to the p-value of the robust linear regression, analyzed metals can be classified into two groups. The first group comprised the metals positively correlated with Ag, namely Zn, Pb, Cu and Cd, and the second group by the metals positively correlated with Au, namely As, Sb, Ge and W. No additional correlations have been observed between the remaining analyzed elements and the metals of both groups. The relative abundances of Zn and Pb can be expressed as simple ratios (e.g. Pb/Zn) or as the zinc ratio 100*Zn/(Zn + Pb), defined by Huston and Large (1987) for massive sulfide systems. Huston et al. (2006) extended the use of this ratio to Zn–Pb–Ag ore deposits. According to these authors the zinc ratio is controlled mostly by metal solubilities in the ore fluid and the metal content of the source rocks, establishing relationships between temperature and salinity of the fluids and the zinc ratio of whole-ore composition. In the Patricia ore deposit, the zinc ratio of mineralized veins ranges from 37.3 in galena-rich samples to 92.8 in sphalerite-rich samples, although the average is 64.4 (standard deviation, 13.81). The Ag:Zn ratio ranges from 0.001 to 0.016 with an average of 0.005 (1:206). The Au content is below 1 ppm in all samples and the Ag:Au ratio ranges from 200 to 6000 (average, 1300).

7. Fluid inclusions microthermometry and LA-ICP-MS

Fluid inclusion assemblages (FIAs) have been studied in quartz from the pre-ore stage (Qz1) and post-ore stage (Qz3), and sphalerite (Sp2A and Sp2B) from the base-metal and Ag stage. According to Bodnar (2003) and Goldstein and Reynolds (1994) a FIA refers to a group of fluid inclusions that were all trapped at the same time. Assuming that all of the fluid inclusions within a FIA show the same room temperature phase ratios and microthermometric behavior, one can assume that the inclusions record the original trapping conditions. Fluid inclusions at the Patricia deposit are systematically liquid-rich at room temperature and do not contain recognizable CO_2. Both primary and secondary fluid inclusions have been identified in the system. Primary fluid inclusions are distributed along growth zones (Fig. 12a–c) and represent the

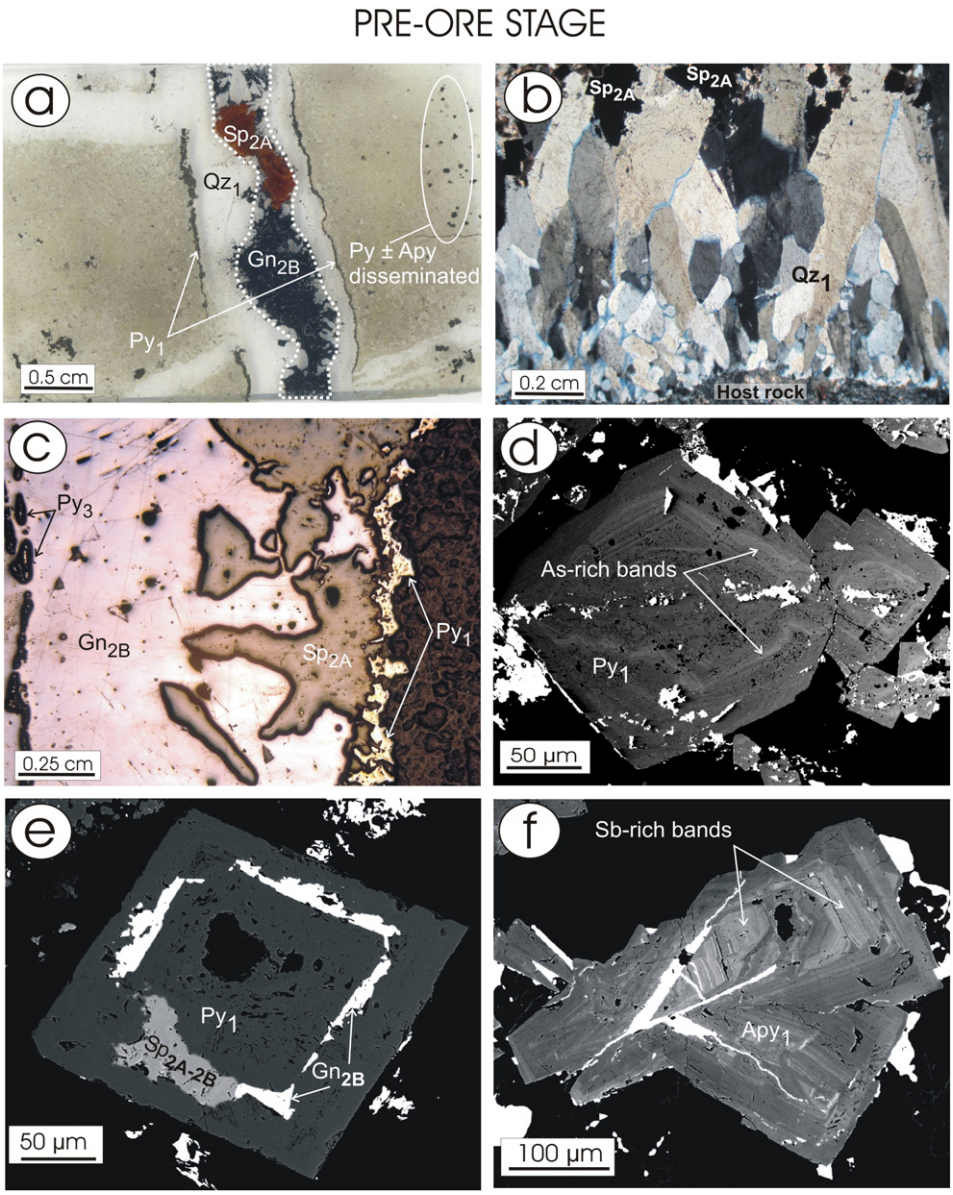

Fig. 7. Photomicrographs of pre-ore stage samples; (a) detailed photograph of a thin section showing the typical occurrence of Py_1 near the vein-wallrock contact, (b) photomicrograph in transmitted light, crossed-polar, showing the typical "comb" texture of quartz (Qz_1), (c) reflected light photomicrograph, one polar, showing Py_1 at the contact between the host rock and the mineralized vein. EPMA photomicrographs; (d) zoned idiomorphic grain of Py_1 with As-rich bands, (e) Py_1 grain being replaced by galena and sphalerite, (f) zoned idiomorphic grain of Apy_1 with Sb-rich bands. Abbreviations: *Qz* = quartz, *Py* = pyrite, *Apy* = arsenopyrite, *Gn* = galena, *Sp* = sphalerite.

fluid from which the host mineral precipitated. Secondary fluid inclusions (Fig. 12d) occur along fracture planes and represent fluids trapped after host-mineral precipitation. Fluid inclusions whose origin is not clearly primary or secondary have only been incorporated in the paragenesis when they show specific features that constrain the time of trapping (i.e. such as when a fluid inclusion forms around a chalcopyrite bleb within sphalerite, indicating that the inclusion and chalcopyrite are coeval; Fig. 12e).

7.1. Pre-ore stage

A total of 39 fluid inclusions (9 FIAs) were studied in Qz_1 (Fig. 7b) located at the outer bands of symmetric mineralized veins. Fine-grained Qz_1 crystals occurring at and close to the vein walls do not contain fluid inclusion suitable for being studied. Therefore, fluid inclusion data were obtained in Qz_1 larger crystals occurring vein inwards as comb-type quartz grains and in close proximity to the stage 2 base-metal sulfides. Primary FIAs are scarce (Fig. 12a–b) whereas secondary trails of FIAs are common but the inclusions in the FIA are smaller than those in FIAs containing primary fluid inclusions (Fig. 12d). Salinities estimated from primary FIAs range from 22 to 6 wt.% NaCl and from secondary FIAs vary from 15 to 3 wt % NaCl. Homogenization temperatures (Th) from primary FIAs range from 236 to 205 °C and from 270 to 165 °C for secondary FIAs (Table 4). Both primary and secondary FIAs frequently contain a fibrous mineral with distinct Raman peaks at 204, 262, 355, 395, 466, 698, 798 and 1167 cm^{-1}, suggesting that the fibrous mineral is a hydrous phyllosilicate, interpreted as illite (Fig. 12b).

7.2. Base-metal and silver stage

A total of 62 fluid inclusions (13 FIAs) were studied in sphalerite, Sp_{2A} and Sp_{2B}, of the substages 2A and 2B, respectively. FIAs in Sp_{2A} are common, usually showing elongated fluid inclusions along growth bands in zoned sphalerite (Fig. 12c). Primary fluid inclusions are usually larger than secondary inclusions, which commonly form trails cross-cutting growth bands within the Sp_{2A}. Salinities estimated from primary

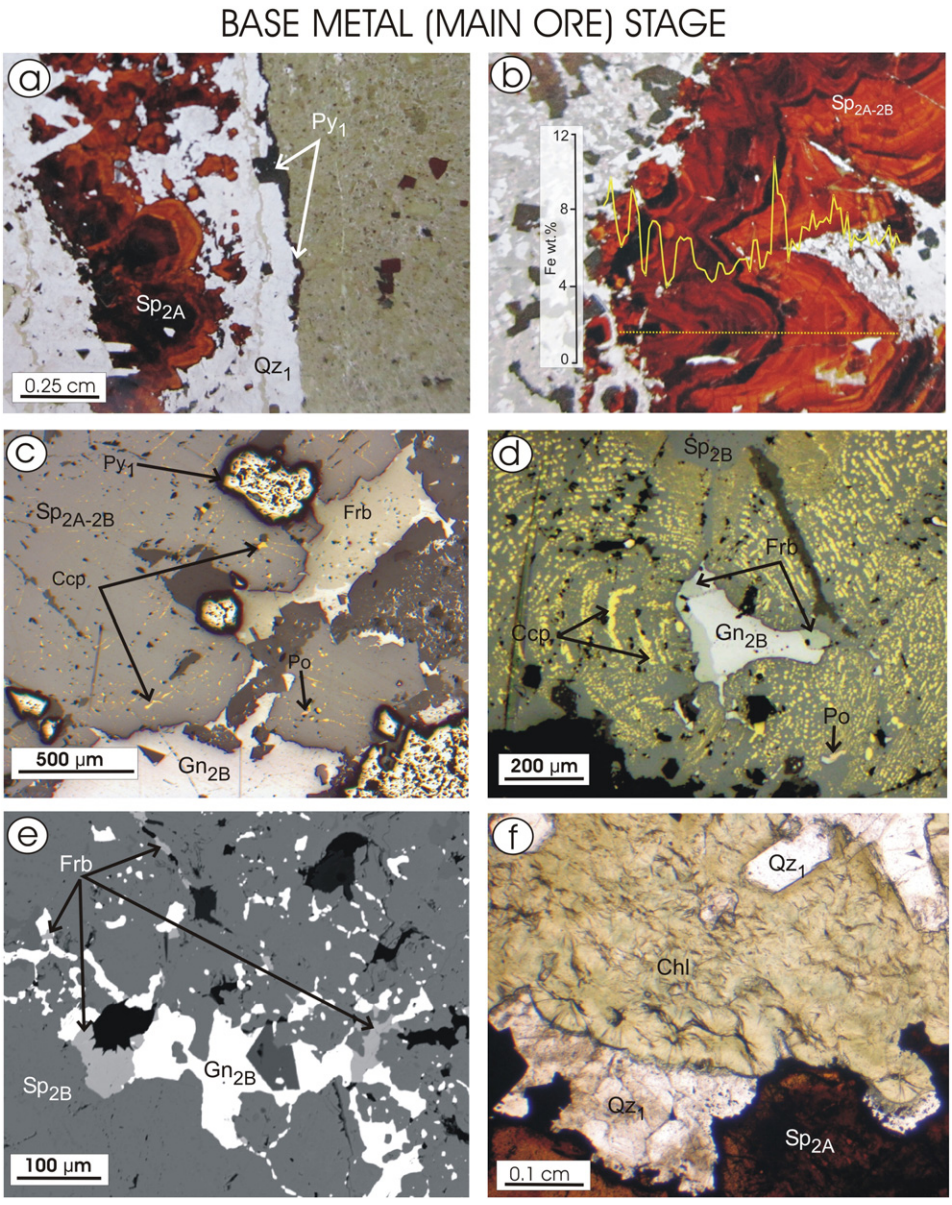

Fig. 8. Photographs of samples from de base-metal and silver stage: (a) detailed photograph of a thin section showing zoned sphalerite grains, Sp_{2A}, within a symmetrical vein, (b) Fe concentration map superimposed onto a grain of Fe-zoned sphalerite, Sp_{2A}. (c–d) photomicrographs in reflected light, one polar, showing the typical texture of the sphalerite, Sp_{2B}, in relationship to chalcopyrite, galena, pyrrhotite and freibergite, (e) EPMA photomicrographs showing the typical distribution of Ag-bearing mineral within galena and filling voids between sphalerite, (f) Photomicrographs in transmitted light, one polar, showing chlorite at the contact with sphalerite. Abbreviations: *Sp* = sphalerite, *Py* = pyrite, *Frb* = freibergite, *Gn* = galena, *Ccp* = chalcopyrite, *Po* = pyrrhotite, *Chl* = chlorite and *Qz* = quartz.

FIAs of substage 2A range from 9 to 1 wt.% NaCl and for secondary FIAs from 4 to 3 wt.% NaCl. Homogenization temperatures (Th) from primary FIAs range from 248 to 172 °C and from 197 to 195 °C for secondary FIAs (Table 4). FIAs in Sp_{2B} were more difficult to study than those in Sp_{2A}, because Sp_{2B} is more Fe-rich and darker, hindering the identification of fluid inclusions (Fig. 12e). Fluid inclusions observed in Sp_{2B} are commonly associated with solid inclusion of minor sulfides such as chalcopyrite, pyrrhotite and Ag-bearing minerals (Fig. 12e). Salinity values from primary FIAs range from 10 to 2 wt.% NaCl and Th from 182 to 138 °C.

7.3. Post-ore stage

A total of 19 fluid inclusions (4 FIAs) were studied in large mosaic-textured Qz_3 quartz crystals. Fluid inclusions were not observed in earlier microcrystalline Qz_3 crystals. Primary fluid inclusions are observed in the growth bands of quartz but their dark color makes them impossible to study (Fig. 12f). FIAs consisting of clear primary inclusions rarely occur (Fig. 12g). These fluid inclusions are commonly small (~10 µm), reporting salinity from 8 to 4 wt.% NaCl and Th ranging from 215 to 175 °C (Table 4). Many secondary inclusions along fractures could be observed in Qz_3 (Fig. 12h) but only some could be studied because of their small sizes. FIAs of secondary inclusions have lower salinity, ranging from 4 to 2 wt.% NaCl and Th ranging from 242 to 150 °C (Table 4). As observed in Qz_1, these FIAs have also trapped illite crystals.

LA-ICP-MS analyses were carried out on 46 individual inclusions. Fluid inclusions in quartz (stages 1 and 3) contain measurable concentrations of Na and commonly contain measurable concentrations of K, Ca, Al and Sb. However, Al and Sb concentrations may reflect contributions from the host quartz. Measurable concentrations of Fe are detected in 6 individual inclusions, and measurable concentrations of Mg, Zn and Pb in 4 individual inclusions. Ag, As, Au, B, Cd, Cu, Ge, Re, Se and Te are below the detection limit in all fluid inclusion in quartz. The Na content ranges from 5 to 340 ppm for inclusions in quartz. In these

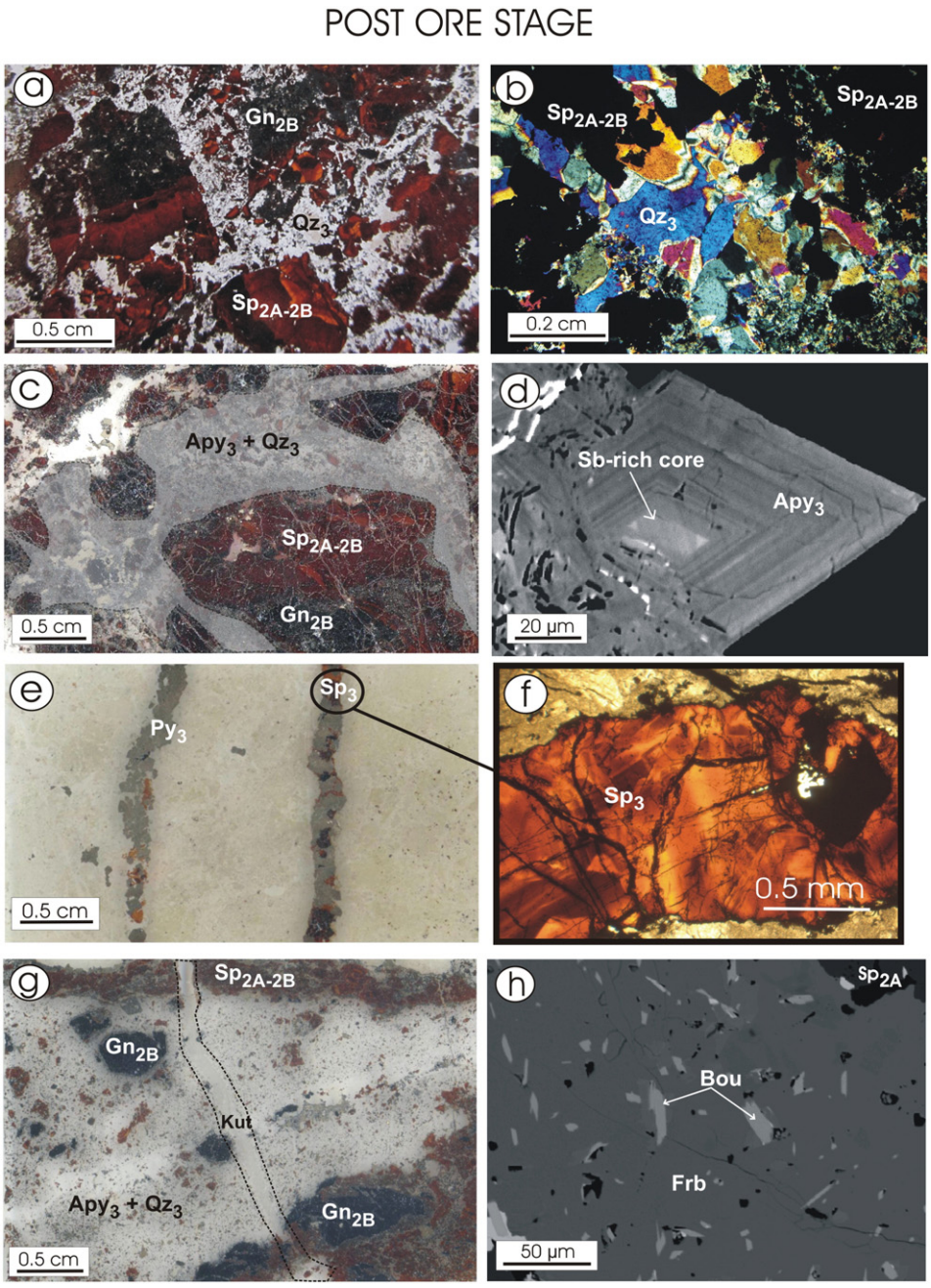

Fig. 9. Photographs of post-ore stage samples: (a) detailed photograph of a thin section (DPTS) showing the typical brecciated texture of sulfides cemented by quartz. (b) Photomicrograph with transmitted light, crossed-polar, showing mosaic (jigsaw)-textured quartz as a cement of the brecciated sulfides. (c) DPTS showing the distribution of Qtz_3 and Apy_3 cementing brecciated sulfides. (d) EPMA photomicrograph of an oscillatory zoned grain of arsenopyrite, Apy_3, with a Sb-rich core. (e) DPTS showing thin vein of pyrite, Py_2, and sphalerite, Sp_3, with the presence of (f) zoned sphalerite crystals. (g) DPTS showing a late-vein of Kut crosscutting Qz_3 and the brecciated sulfides. (h) EPMA photomicrograph of a lead sulfosalt (boulangerite) within a silver sulfosalt (freibergite). Abbreviations: *Frb* = freibergite, *Apy* = arsenopyrite, *Bou* = boulangerite, *Gn* = galena, *Kut* = kutnohorite, *Qz* = quartz, *Py* = pyrite, *Sp* = sphalerite.

inclusions, concentrations of Ca range from 2.2 to 183 ppm, K from 1.3 to 125 ppm and Fe from 1 to 10 ppm. Strong correlation was observed between the Na content with Ca, K and Fe contents and salinity calculated by microthermometry.

Fluid inclusions in sphalerite (stages 2A and 2B) also contain measurable concentrations of Na and commonly contain measureable concentrations of K, Ca, Cd, Cu, Fe and Zn. However, Cd, Cu, Fe and Zn concentrations may reflect contributions from the host sphalerite. Measurable concentrations of B (up to 14 ppm) are detected in 10 individual inclusions. Ag, Al, As, Au, Ge, Mg, Pb, Re, Se, Si and Te are below the detection limit in all fluid inclusions in sphalerite. The Na content ranges from 3 to 73 ppm for inclusions in sphalerite. In these inclusions, concentrations of Ca and K range from 1.3 to 43 ppm and from 1.2 to 23 ppm, respectively. Strong correlation was observed between the Na content with Ca and K contents and salinity calculated by microthermometry.

8. Discussion

8.1. Tectonic framework

The Patricia epithermal ore deposit was developed in an active tectonic system, as shown by its structural features and internal vein textures. The main faults in the area strike N10–30W, whereas the synthetic Riedel faults lie N50–70W. The extensional vector was located ~N-S, as indicated by the mineralized structures occurring as parallel

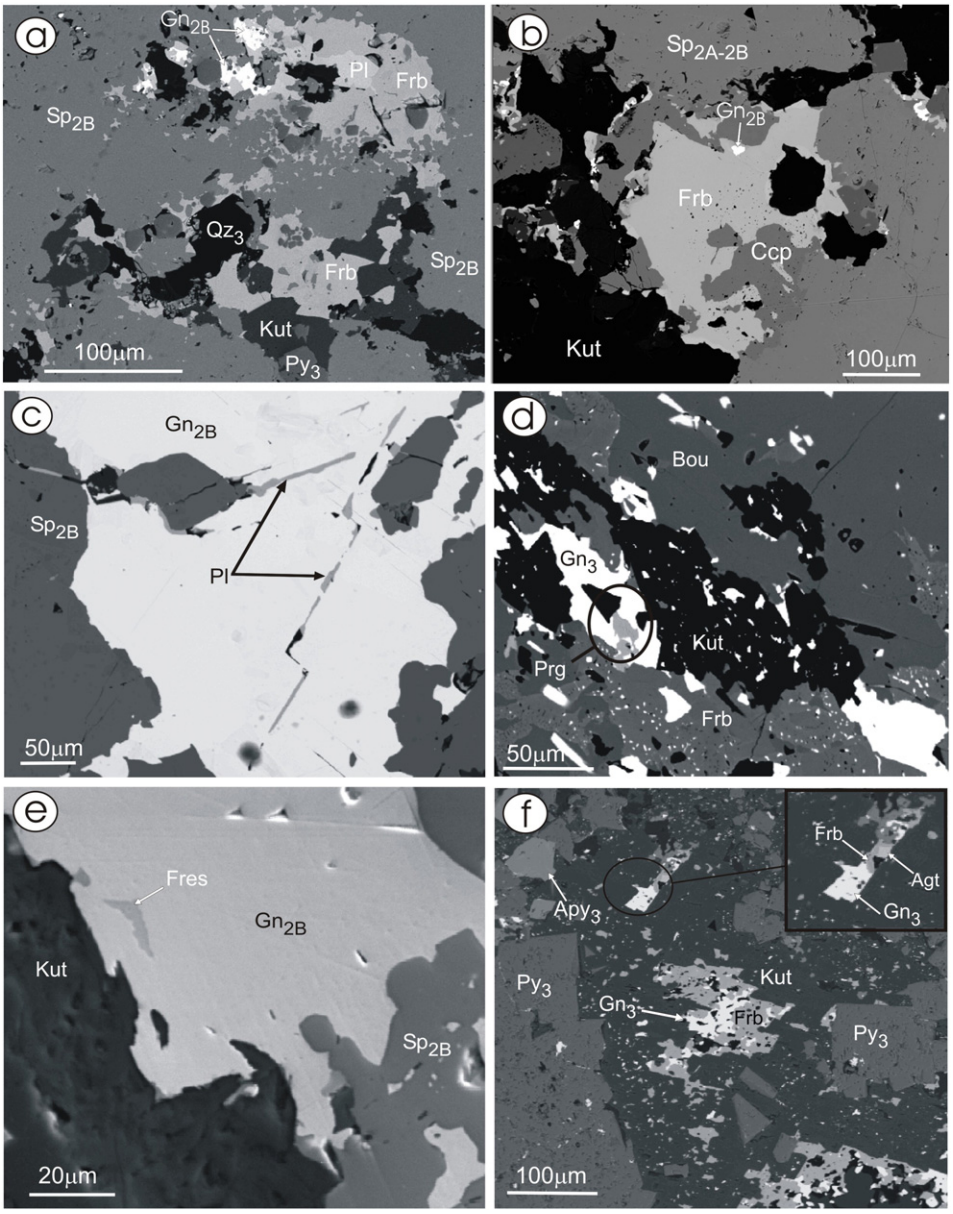

Fig. 10. Scanning Electron Microscope photomicrographs: (a) Ag-bearing minerals filling spaces among aggregates of sphalerite grains; EPMA photomicrographs: (b) freibergite filling spaces between sphalerite grains in close association with chalcopyrite, galena and kutnohorite (c) elongated polybasite grains within galena (d) boulangerite, freibergite and pyrargyrite within galena and kutnohorite filling voids in sphalerite (e) freieslebenite within galena (f) tiny acanthite grain and freibergite within galena in a kutnohorite matrix. Abbreviations: *Agt* = acanthite, *Bou* = boulangerite, *Ccp* = chalcopyrite, *Fres* = freieslebenite, *Frb* = freibergite, *Gn* = galena, *Kut* = kutnohorite, *Pl* = polybasite, *Py* = pyrite, *Prg* = pyrargyrite, *Sp* = sphalerite.

vein systems, E-W- to ENE-WSW-oriented, with stockwork veinlets occurring along NW-SE, NE-SW and E-W orientations. These features indicate that the mineralization formed under a sinistral strike-slip regime, which controlled the development of the mineralized structures and created open spaces where the mineralization was deposited. In fact, transtensive domains with pull-apart and generalized extensional structures are suggested, as shown by the infilling of veinlets of different orientations forming the stockwork. Furthermore, these veinlets were continuously formed and/or repeatedly opened during the mineralization process as indicated by different types of veinlets recognized in the deposit (Fig. 5), often showing open space filling textures, i.e. symmetrical banding, crustification, quartz comb structures. A strike-slip structural framework has been also described in other epithermal deposits, such as the Pallancata deposit (Gamarra-Urrunaga et al., 2013) and the Shila-Paula district in Peru (Chauvet et al., 2006), the Faride deposit in the Antofagasta region, Chile (Camus and Skewes, 1991) and the Gandy and Abolhassani prospects in Iran (Shamanian et al., 2004). In these deposits, the kinematics of the strike-slip structures also controlled mineral deposition in parallel vein systems.

At a regional scale, the Patricia ore deposit is located in the Precordillera domain, which occupied the Andean back-arc region during the Cretaceous (Mpodozis and Ramos, 1990). The main contractional deformation event recorded in the Precordillera took place in the Eocene (Incaic Phase; Noble et al., 1979). This event was coeval with the initial formation of the still active Bolivian orocline (Isacks, 1988; Allmendinger et al., 2005; Arriagada et al., 2008; Capitanio et al., 2011), whose southern limb has since been subjected to clockwise rotation accommodated by sinistral strike-slip along trench-parallel fault systems, e.g. the Domeyko fault system. The Patricia deposit is located at the northern end of this fault system. These regional constraints are in agreement with the features observed at the Patricia deposit and in nearby rock units. The overall deformation of the host-rocks is compatible with the sinistral transpressional regime during the Incaic Phase in this part of the Andes. The sinistral regime that is also inferred from the

Table 3
Bulk rock analyses from mineralized veins in the Patricia ore deposit. *b.d = below detection limit.

Samples	d.l	Units	1	2	3	4	5	6	7	8	9	10
Cu	0.5	ppm	59	23.9	48.6	115.6	14.2	99.4	40.8	26.5	89.7	19.9
Zn	1	ppm	11757	7286	10304	2919	2165	23597	8155	6047	12903	9423
Ag	0.01	ppm	34.31	20.87	33.75	48.03	18.42	68.3	25.91	25.48	42.36	9.56
Cd	0.02	ppm	84.53	43.42	79.08	15.22	11.52	168.87	47.76	35.65	82.92	11.5
In	0.005	ppm	0.065	0.02	0.054	0.065	0.056	0.056	0.054	0.054	0.067	0.044
As	0.5	ppm	215.2	13257	2107.2	457.2	1142.7	7758	14842	13363	8911	982.3
S	0.01	wt.%	6.16	11.66	2.96	3.71	7.39	8.83	6.18	8.66	11.8	1.94
Sb	0.05	ppm	68.16	200.56	82.98	102.99	43.06	177.76	579	213.77	235.53	38.1
Se	0.5	ppm	0.7	6.2	2.5	b.d	2.7	3.5	2.4	3.2	1.3	2.1
Pb	0.5	ppm	5717	3166	4592	1969.7	3635	13265	4775	4967	6512	732.5
Bi	0.01	ppm	0.13	0.86	0.42	1.03	0.08	0.3	0.17	0.33	0.41	0.84
Te	0.05	ppm	b.d	b.d	b.d	b.d	b.d	0.59	b.d	0.37	b.d	b.d
Co	0.1	ppm	17.5	16.7	8.9	15	12.2	22.3	8.4	14.4	8.7	27.7
Mo	0.1	ppm	1	0.7	0.9	0.8	0.6	3.3	0.6	0.7	0.8	10.1
Au	1	ppb	10	85	30	8	65	79	162	129	106	36
Ge	0.05	ppm	0.97	0.85	0.96	0.85	0.81	1.06	1.35	1.35	1.24	1.05
W	1	ppm	2	21	14	5	9	17	22	26	21	4

structural characteristics of the deposit itself suggests that it may have been formed during later, post-folding stages within the same Incaic Phase or, alternatively, during a post-Incaic event with similar kinematics. Whichever the case, the deposit was exhumed by the time of eruption of the ignimbrite sequence that unconformably overlies its southern part (Fig. 2b). In the absence of absolute ages for both the mineralization and the unconformable ignimbrites no further constraints on the timing are possible. However, the above discussion reinforces the inclusion of the Patricia deposit within the late Eocene–early Oligocene metallogenetic belt. This interpretation is supported by the Patricia geographical position (Fig. 1b), its proximity to the early Oligocene Queen Elizabeth porphyry copper deposit (Davidson and Mpodozis, 1991) and its genetic, geometrical and kinematic relationships to the Domeyko fault system, which is spatially and temporally coincident with the development of the metallogenic belt (Sillitoe and Perelló, 2005; Sillitoe, 2010; and references therein).

The Patricia ore deposit is divided along its central part into two blocks (eastern and western) separate from each other by a set of NNW-ESE-trending reverse faults. The kinematic movement on these faults resulted in uplift of the eastern block (Fig. 3a), exhuming thicker and deeper parts of the deposit, as confirmed by fluid inclusion data (see below). In contrast, a shallower part of the system is exposed in the western block as suggested by the occurrence of cherts, cryptocrystalline silica and jasperoids (Fig. 3e–f), which are absent in the eastern block. These siliceous formations are typical of thermal spring settings (Camprubí et al., 2006a, 2006b).

8.2. Temperature and mechanisms of ore deposition

Based on the internal textures of veinlets and cross-cutting relationships among them, three main mineralizing stages have been recognized in the Patricia deposit, with the second stage being the most economically significant. The paragenesis of each stage and the evolution of the mineralizing fluids (Fig. 13) both indicate changes in mineralizing conditions over time.

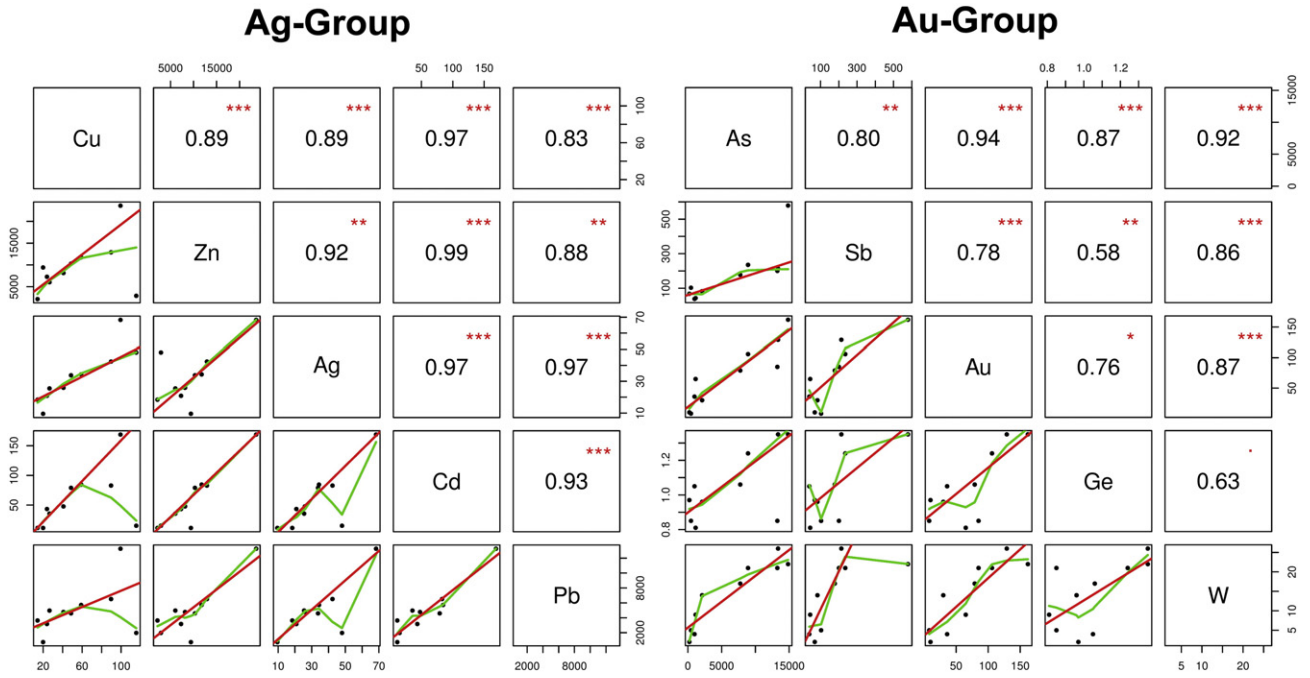

Fig. 11. Matrix of scatterplots of the two groups of elements (Ag and Au groups) with positive correlations calculated from whole-ore composition of the mineralized veins. Lower panels contain the scatterplot of each pair of elements, the model of the robust linear regression (red) and the Tukey smoothing line (green). Upper panels contain the r squared coefficient and the level of significance of the robust linear regression (*** = 0.999; ** = 0.99; * = 0.95; · = 0.90). Units are in ppm except for Au which is in ppb.

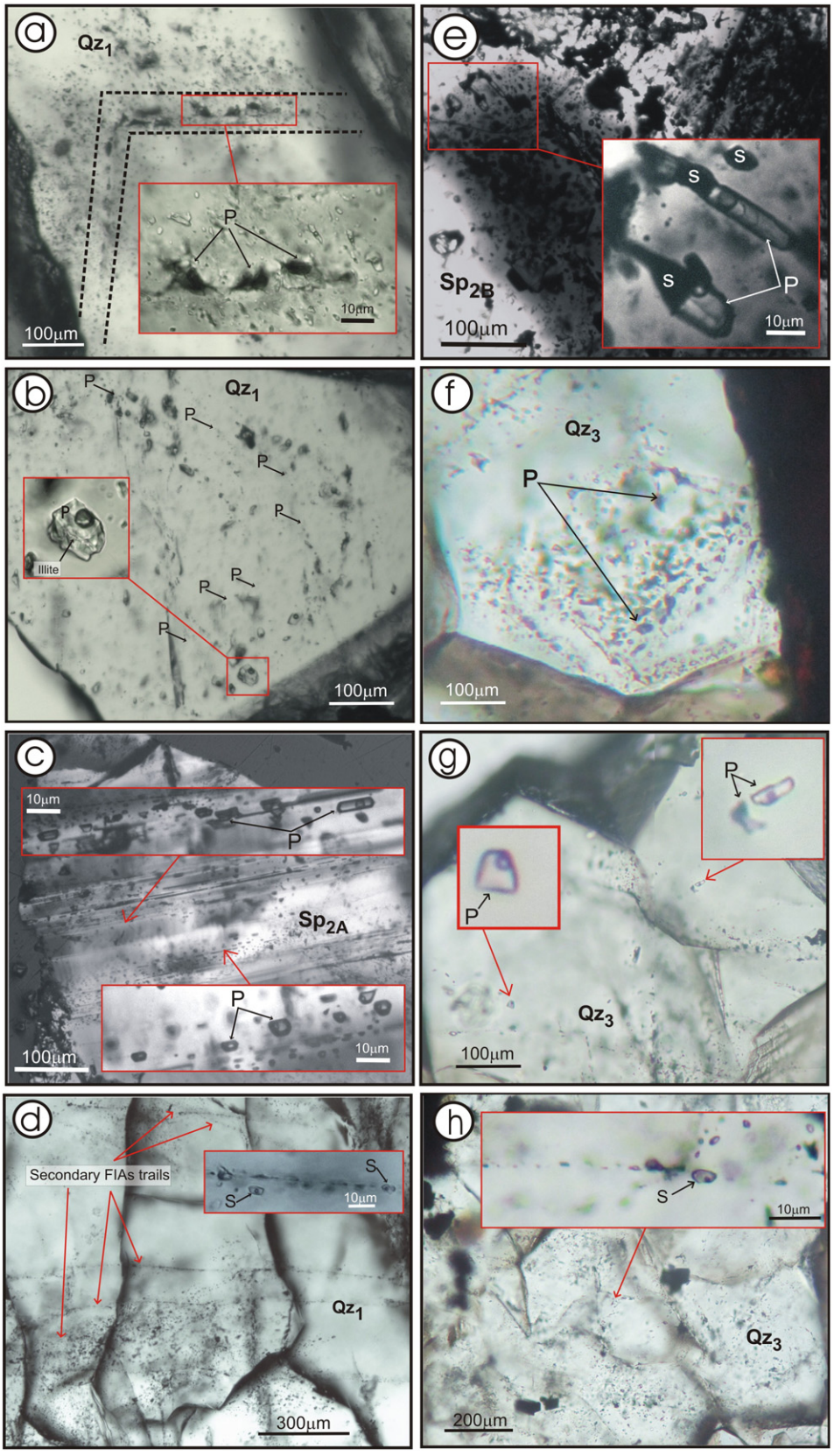

Fig. 12. Photomicrographs of fluid inclusion assemblages (FIAs) of the three main stages of mineralization: (a–b) Primary FIAs in growth bands of quartz (Qz_1). (b) Detail of fibrous hydrous phyllosilicate, likely illite, trapped within a primary fluid inclusion. (c) Primary FIAs in Sp_1 distributed in parallel growth bands of Sp. (d) Secondary FIAs occurring as parallel trails in Qz_1. Note that these inclusions are smaller than primary ones. (e) Primary FIAs in Sp_{2B} characterized by the presence of chalcopyrite and Ag-sulfosalt inclusions. (f) Dark primary FIAs distributed in parallel growth bands of Qz_3. (g) Individual groups of primary FIAs in Qz_3. (h) Several trails of secondary FIAs in Qz_3.

Table 4
Microthermometric results from each fluid inclusion assemblage (FIA) in quartz and sphalerite from each mineralization stage in the Patricia ore deposit.

Sample	Vein	Level (m)	Stage	Host mineral	Type	FIA	No.	T_h range (°C)	Avg	Salinity range (% NaCl)	Avg	Solid inclusions
PT105-177,60	Catedral	145.8	1	Quartz	P	1p1	3	220–231	225	6.4–16.6	12.7	–
PT109-235,85	Catedral	204.3	.	.	.	1p2	2	228–236	232	7–9.3	8.2	Ilite
PT96-161	Catedral	117.7	.	.	.	1p3	8	205–236	224	14.0–21.5	20	Ilite
PT96-158,70	Catedral	116.0	.	.	S	1s1	3	248–269	256	4.0–4.6	4.3	Ilite
PT96-161	Catedral	117.7	.	.	.	1s2	4	165–175	172	12.0–15.4	13.1	–
PT109-235,85	Catedral	204.3	.	.	.	1s3	8	245–252	248	1.7–1.5	6.2	Ilite
PT73-115.95	Catedral	93.8	2A	Sphalerite	P	2p1	4	205–214	211	7.4–9.1	8.6	–
PT73-115.95	Catedral	93.8	.	.	.	2p2	5	173–186	177	2.1–2.7	2.4	–
PT73-115.95	Catedral	93.8	.	.	.	2p3	3	202–232	222	5.7–5.9	5.8	–
PT96-199,20	Catedral	145.7	.	.	.	2p4	7	176–200	185	1.2–2.2	1.8	–
PT96-199,20	Catedral	145.7	.	.	.	2p5	5	190–201	193	5.0–6.4	5.7	–
PT96-199,20	Catedral	145.7	.	.	.	2p6	2	172–196	184	5.0–5.4	5.2	–
PT105-182,80B	Catedral	149.7	.	.	.	2p7	3	177–178	177	5.4–6.9	6	–
PT105-182,80A	Catedral	149.8	.	.	.	2p8	9	207–212	208	4.0–4.6	4.5	–
PT96-199,20	Catedral	145.7	.	.	.	2p9	6	240–248	244	4.3–5.1	4.8	–
PT105-183,20	Catedral	150.0	.	.	.	2p10	6	189–198	192	2.7–4.5	3.5	–
PT96-199,20	Catedral	145.7	.	.	S	2s1	2	196–197	196	3.1–3.4	3.2	–
PT73-241,40	Carlos	195.3	2B	.	P	2bp1	7	168–182	173	2.2–7.3	5	–
PT109-263,40	Catedral	228.1	.	.	.	2bp2	5	134–168	149	5.6–9.5	7.6	–
PT96 - 199,20	Catedral	145.7	3	Quartz	P	3p1	3	172–186	179	7.2–8.1	7.7	–
PT96 - 199,20	Catedral	145.7	.	.	.	3p2	5	190–216	201	2.1–5.9	5	–
PT73-115,90	Catedral	93.8	.	.	S	3s1	9	227–242	235	2.1–2.9	2.5	Ilite
PT96 - 199,20	Catedral	145.7	.	.	.	3s2	2	148–149	149	3.6–4.2	3.9	Ilite

8.2.1. Pre-ore stage

The pre-ore stage is defined by an early quartz Qz_1 coexisting with pyrite Py_1 and arsenopyrite Apy_1. Quartz grain size increases from vein walls inwards, where quartz crystals are often prismatic, thus indicating a progressive decrease in silica super saturation as precipitation of quartz proceeded. Primary fluid inclusions studied in coarse-grained Qz_1 indicate a wide range of salinities, from high salinity close to the NaCl saturation at room temperature to 6 wt.% NaCl, and homogenization temperatures from 236 to 205 °C. However, the lack of microthermometric data from fine-grained Qz_1 does not allow knowing the fluid features during the early pre-ore stage. The salinity and temperature range obtained for the late pre-ore stage is in general agreement with fluid inclusion data from other intermediate sulfidation epithermal deposits (Bodnar et al., 2014). The observed salinity variation within this stage strongly suggests a process of mixing between brine and a more diluted fluid (Fig. 13). This stage is similar to the initial stages in other epithermal deposits where quartz, pyrite ± arsenopyrite are typically deposited during the earliest stages at the highest temperatures (e.g. El Bronce deposit, Camus et al., 1991; San Cristóbal deposit, Phillipson and Romberger, 2004; La Guitarra deposit, Camprubí et al., 2006a, 2006b; Caylloma district, Echavarria et al., 2006). The frequent presence of illite trapped within fluid inclusions in Qz_1 (Fig. 13) indicates that pre-ore stage mineralization took place under slightly acidic conditions, because illite is formed at pH from 5.8 to 6.3 (Romberger, 1991) and temperatures from 220 to 300 °C (Henley and Ellis, 1983; Reyes, 1990), which are compatible with the obtained homogenization temperatures of the pre-ore stage fluid inclusions. Py_1 and Apy_1 are commonly zoned showing alternating As-rich and Sb-rich bands, respectively. This may reflect slight compositional variations of the mineralizing solutions as an expression of disequilibrium and metastable conditions, as is commonly observed in epithermal deposits (e.g. Carrillo-Rosúa et al., 2008).

8.2.2. Base-metal and Ag-bearing minerals stage

The main mineralizing event observed in the Patricia deposit is deposition of two generations of sphalerite (Sp_{2A} and Sp_{2B}), galena

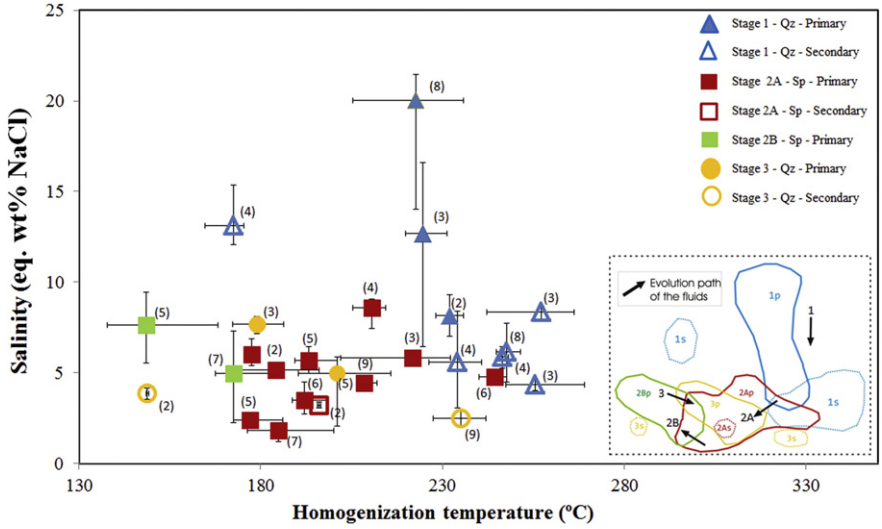

Fig. 13. Range in measured homogenization temperature and salinity of individual fluid inclusion assemblages (FIAs) observed in the Patricia ore deposit. Each data point corresponds to the average homogenization temperature and salinity for the fluid inclusion assemblage and the error bars represent the minimum and the maximum values for each FIA. A possible evolution path of the mineralizing fluids in the deposit is shown in the lower right corner (n) Number of fluid inclusions in each FIA.

(Gn_{2B}) and minor amounts of pyrite, chalcopyrite, Ag-sulfosalts and trace of pyrrhotite within Sp_{2B}. Primary fluid inclusions studied in Sp_{2A} and Sp_{2B} indicate lower salinity (2–10 wt.% NaCl) and lower homogenization temperatures than in the pre-ore stage. Stage 2 is characterized by a gradual cooling from 250 to 140 °C at constant low to moderate salinity. Ag-bearing phases mainly occur at the end of this stage at temperatures ranging from 180 to 140 °C. The temperatures indicated by fluid inclusions for the substage 2B are in agreement with those estimated using freibergite as geothermometer. This geothermometer is based on the isotherms calculated by Sack (2005) using the molar Ag/(Ag + Cu) and Zn/(Zn + Fe) ratio of freibergite (Fig. 14). The geothermometric analyses of freibergite, which is the most abundant Ag-bearing phase in the Patricia deposit, suggest that most of the silver mineralization took place in the interval from around 230 to less than 170 °C, with most of the data plotting below the 170 °C isotherm. Moreover, the occurrence of minor stephanite in the substage 2A also marks another upper limit for Ag deposition at 197 ± 5 °C (e.g. Keighin and Honea, 1969; *Pallancata deposit*, Gamarra-Urrunaga et al., 2013). Freibergite compositions giving temperatures above 200 °C could represent re-equilibrated phases due to late higher temperature fluids that characterize the post-ore stage (Fig. 13) (see below). In addition, the data in Fig. 14 support the existence of a miscibility gap in fahlores first predicted by O'Leary and Sack (1987) and confirmed by Sack (2005) and Chutas and Sack (2004).

Precipitation of ore minerals due to decreasing temperature in hydrothermal systems is generally the result of either conductive loss of heat from the system or from mixing with a lower temperature fluid (Leach and Corbett, 2008). Cooling has also been described in some deposit as the main deposition process (e.g. San Cristobal deposit, Phillipson and Romberger, 2004) or as one of several mechanisms as boiling or fluid mixing (e.g. Faride deposit, Camus and Skewes, 1991; El Barqueño and La Guitarra deposits, Camprubí et al., 2006a, 2006b). Evidence in the Patricia deposit suggests that a combination of both mixing and cooling likely occurred. As stated earlier, a decrease in fluid salinity between stage 1 and stage 2 suggests possible dilution of an early brine due to mixing with a lower salinity fluid (e.g. Einaudi et al., 2003; Sillitoe and Hedenquist, 2003; Simmons et al., 2005). However, cooling seems to be the most important process responsible for the main stage of ore precipitation, as shown by fluid evolution during stage 2. The LA-ICP-MS data from fluid inclusions also show evidence of dilution because the Na, Ca and K contents decrease from stage 1 to stage 2. In addition, the model proposed by Sack (2005) for Ag–Pb–Zn deposits, implying a primary high-temperature, high-Ag-galena phase that breaks down during cooling and gives rise to the silver mineralization, provides a reasonable reference for the Patricia deposit, which agrees with the cooling process recorded by fluid inclusions.

Sulfur and oxygen activities of the fluids during stage 2 have been estimated from the composition of sphalerite in equilibrium with pyrite according to Barton et al. (1977). The composition of Sp_{2A} and Sp_{2B} in equilibrium with pyrite ranges from 6 to 15 mol% FeS and plots within the sulfide dominant field in the sulfur vs. oxygen activity diagram (Fig. 15). Accordingly, sphalerite precipitated from a fluid with sulfur activity between −12.2 and −12.5 and oxygen activity around −38. Additionally, the stability limits for Ag-bearing and Pb-bearing minerals have been obtained of the sulfur activity vs temperature diagram from Jasinski (1983).

8.2.3. Post-ore stage

The post-ore stage is defined by the deposition of quartz (Qz_3), pyrite (Py_3) and arsenopyrite (Apy_3), minor sphalerite and galena and the final precipitation of minor kutnohorite and trace amounts of Ag-bearing and Pb-bearing minerals. Primary fluid inclusions studied within Qz_3 indicate higher temperatures (215–175 °C) and similar salinity (8–2 wt.% NaCl) compared to the previous substage 2B (Fig. 13).

The rise in the temperature of the circulating fluids from stage 2B to stage 3 could have been as much as 75 °C. This fact poses two important questions: 1) did fluid inclusions in sphalerite Sp_{2A} and/or Sph_{2B} re-equilibrate during the post-ore stage? and, therefore 2) are the obtained microthermometric data reliable? As pointed out by Bodnar and Bethke (1984), overheating of sphalerite may cause the fluid inclusions to stretch, leak or decrepitate, thus yielding incorrect microthermometric

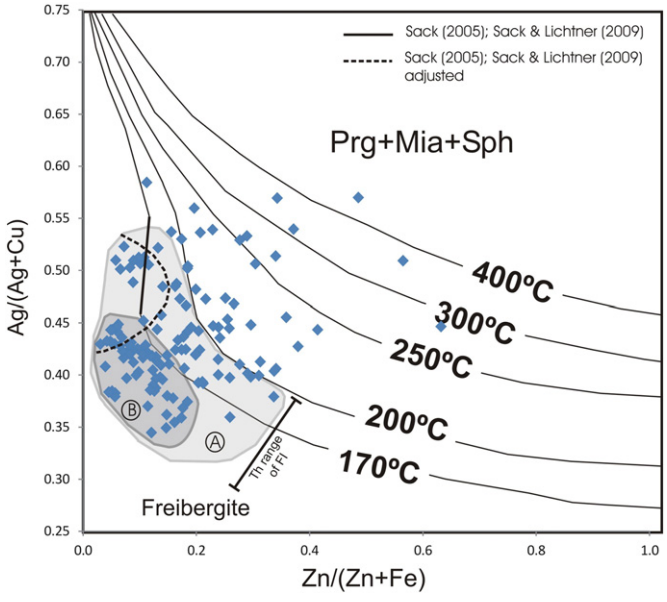

Fig. 14. Molar Ag/(Ag + Cu) and Zn/(Zn + Fe) concentration of freibergite from the Patricia ore deposit compared with the maximum solubility of Ag in freibergite in the system Ag_2S–Cu_2S–ZnS–FeS–Sb_2S_3 at 170, 200, 250, 300, and 400 °C [freibergite in equilibrium with pyrargyrite (Prg), sphalerite (Sph), and miargyrite (Mia)] modified from Sack (2005). It is also shown, with a solid line, the approximate miscibility gap for fahlores for the 170 °C isotherm calculated by Sack (2005) and, with a dashed black curve, the approximation for the polythermal miscibility gap intersection with the isotherms and translated it downwards in Ag/(Ag + Cu) ratios while maintaining the width of the gap calculated at 170 °C (adjusted from Sack (2005); Sack and Lichtner (2009)). curve). Two shaded areas (A–B) delimit the areas with the most common freibergite analysis which indicates temperatures <200 °C. The darker shaded area (B) below the 170 °C isotherm shows higher concentration of freibergite. The solid bar shows the range of homogenization temperature (Th) of FI observed in sphalerite containing Ag-bearing minerals from sub-stage 2B.

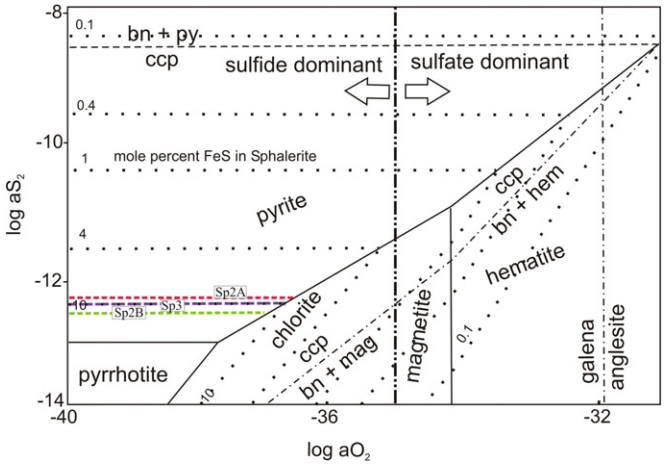

Fig. 15. Activity of sulfur versus activity of oxygen diagram showing the stability fields for the main minerals in the Patricia deposit at 250 °C. Dashed colored lines show the 3 sphalerite assemblages observed in the Patricia ore deposit. Also, shown by the heavy vertical dashed-dot line is the boundary between fields of dominant aqueous sulfur species, H_2S and $NaSO_4$ at a pH = 5.4. Modified from Barton et al. (1977).

data. According to these authors, the amount of overheating necessary to initiate stretching in sphalerite-hosted inclusions depends, among other factors, on the inclusion size and shape, and the confining pressure, ranging from <8 °C for inclusions several hundred μm in diameter to >75 °C for 10 μm-sized inclusions at 1 bar confining pressure. Fluid inclusion sizes in the Patricia sphalerites are usually below 10 μm, and only exceptionally reach 20 μm (i.e. Fig. 12e). Regarding the confining pressure, fluid inclusion data presented in this paper belong to sphalerite from cores samples located at depths below present surface of 95 to 150 m (stage 2A) and 195 to 228 m (stage 2B) which, assuming hydrostatic pressure conditions as indicated by the veins open-space filling textures, correspond to minimum confining pressure around 10–15 bars and 20–23 bars, respectively. These cores were drilled in the uplifted eastern block of the deposit, which exposes a deeper part of the mineralization than the western blocks. This means that an unknown thickness of volcanic mineralized rocks has been already eroded and then, real confining pressures should be higher than the values estimated above (see below for further discussion on depth of ore deposition). According to Bodnar and Bethke (1984), the higher the confining pressure, the greater the amount of overheating required to initiate stretching for a given inclusion volume. Therefore, reequilibration of inclusions in sphalerite might have occurred due to the increase of temperature from stage 2A to stage 2B, however the confining pressure was, most probably, high enough to prevent stretching, even in the shallower sphalerite samples (94 m below present surface, see below). Therefore, microthermometric data from sphalerite-hosted inclusions presented in this work are considered fully reliable.

In the post-ore stage, Qz_3, Py_3 and Apy_3 commonly cement the brecciated sulfides of the main-ore stage, so the increase of temperature and similar salinity of the fluids in the post-ore stage were accompanied by brecciation and opening of spaces where the mineralization was ultimately deposited. These breccias indicate either a sharp pressure drop, maybe leading to limited boiling, or just a tectonic process. Boiling is not supported by fluid inclusion observations, and although the lack of fluid inclusion evidence for boiling does not preclude its occurrence, tectonic processes are likely to have occurred given the deposit active tectonic setting. However, according to Fig. 13, cooling is likely to be the main mechanism of mineral deposition in this stage.

The formation of zoned Py_3 and Apy_3 with As-rich and Sb-rich bands, respectively, in equilibrium with Qz_3 suggests compositional variations in fluids similar to those observed in the pre-ore stage. During the final events of the post-ore stage and after precipitation of most sulfides, minor kutnahorite and Ag-bearing minerals such as freieslebenite and acanthite were precipitated. The presence in the late depositional stages of carbonates is a typical characteristic of the latest stages in epithermal deposits (Baumgartner et al., 2008; Canet et al., 2009; Catchpole et al., 2012; Sillitoe and Hedenquist, 2003) as a result of a last fluid pulse after the main mineralizing event. In other epithermal deposits, Ag-bearing minerals commonly precipitate during the last stages (e.g. Baumgartner et al., 2008; Bendezu and Fonboté, 2009; Camprubí et al., 2006a, 2006b; Gröpper et al., 1991; Phillipson and Romberger, 2004; Vassileva et al., 2014) usually due to a combination of different factors involving mixing between magmatic and meteoric fluids, increasing oxygen fugacity and decreasing fluid temperature (Vassileva et al., 2014). Illite is also present as trapped crystals within fluid inclusions in Qz_3. According to several authors (i.e. Romberger, 1991; Moncada and Bodnar, 2012) the pH stability field for illite is around 6, whereas carbonates typically occur within neutral to alkaline conditions. The formation of kutnohorite is comparable to similar phases of Ca/Mn-bearing carbonates described in other epithermal ore deposits, whose deposition is favored by an increase of oxygen fugacity (fO_2) and CO_2 concentration (e.g. Canet et al., 2009; Catchpole et al., 2012; Damian, 2003). Therefore, the formation of kutnohorite in the final post-ore stage suggests that slightly acidic-neutral fluids dominant during previous mineralization stages (from the pre-ore to post-ore stage), evolved at the end of the post-ore stage from neutral to alkaline fluids.

8.3. Whole-ore composition

Statistically significant and positive correlations between Ag–Cd–Cu–Pb–Zn and Au–As–Ge–Sb–W reflect the mineralogical control in the element distribution. The Ag–Cd–Cu–Pb–Zn group is related to base-metal sulfides (sphalerite, galena and chalcopyrite) and Ag-bearing minerals whereas the Au–As–Ge–Sb–W group is related to arsenopyrite and pyrite. The observed positive correlations between the Ag–Cd–Cu–Pb–Zn group support the interpretation that these metals were preferentially deposited during the base-metal stage characterized by precipitation of sphalerite, galena, chalcopyrite and Ag-bearing minerals. The positive correlation between Zn and Cd ($r^2 = 0.99$ and p-value <0.001) is consistent with the fact that Cd substitutes for Zn in sphalerite, as reflected by the presence of trace amounts of Cd in sphalerite (up to 0.3 wt.%). In contrast, the positive correlation between Pb and Ag ($r^2 = 0.97$ and p-value <0.001) is not related to the presence of Ag in galena because EPMA analyses of galena rarely show significant Ag content (~0.1 wt.%). Alternatively, the Pb–Ag correlation in whole-ore composition can be explained by the fact of Ag-bearing minerals and galena are in close textural association with most of the Ag-bearing minerals occurring within galena. This occurrence is in agreement with the possible break down of high-Ag-galena into Ag-free galena and Ag-bearing phases during cooling (as proposed by Sack (2005)) that would further explain the observed Pb–Ag correlation. The mean and standard deviation of the zinc/lead ratio (64.4–13.81, respectively) is in agreement with the predominance of sphalerite in the Patricia deposit.

The strong and positive Sb-As correlation ($r^2 = 0.80$ and p-value <0.01), the wide distribution of these elements in the scatterplot (Fig. 11) and their positive correlations in Py and Apy, all indicate that Sb and As substitute for each other in these minerals. Although Ag-sulfosalts also contain some Sb, the lower relative proportion of these minerals in the whole-ore volume in comparison to arsenopyrite and pyrite probably led to the correlation of Sb with Au and As instead of Ag. The positive Au–As correlation ($r^2 = 0.94$ and p-value <0001), the low Au concentrations in all analyzed samples (<1 ppm) and the absence of discrete Au-bearing minerals suggests that Au may be scarce (ppb or few ppm levels) within arsenopyrite and As-rich pyrite, but this cannot be proven until analysis are carried out on these minerals. The mineralogical control of Au by arsenopyrite or As-rich pyrite has been extensively documented previously (e.g. Huston and Large, 1989; Camus et al., 1991; Genkin et al., 1998; Hedenquist et al., 2000; Einaudi et al., 2003; John et al., 2003; Reich et al., 2005; Sung et al., 2009).

The presence of Fe in both arsenopyrite–pyrite and sphalerite–chalcopyrite explains the absence of statistically significant correlation of Fe with any other metal in the whole-ore composition. The absence of a statistically significant correlation of Se, Bi, Te, Co and Mo with other metals also indicates the lack of mineralogical control for these metals within the paragenetic sequence established in the Patricia deposit.

8.4. Depth of ore deposition and erosion of the eastern block

Minimum depth of ore deposition below the paleowater table in the Patricia deposit can be estimated from hydrostatic boiling point curves (Haas, 1971) given that 1) hydrostatic pressure is indicated by open-space filling textures in the mineralized veins, and 2) there is no evidence for fluid boiling, at least in the pre-ore and main ore stages.

Microthermometric data, sampling depth and theoretical boiling depth (Haas, 1971) for some selected inclusions in Qz_1, Sp_{2A} y Sp_{2B} are shown in Table 5. As indicated previously, fluid inclusions were studied in samples located between 95 m (lower limit of the oxidized zone) and 230 m deep (lower depth reached by drilling) in the deposit eastern block. Minimum depth of ore deposition estimated from boiling curves in this mineralized interval (Table 5) is only significant if it is equal or larger than the sampling depth below present surface (i.e. data from Qz_1 and Sp_{2A}). Thus, ore deposition in the studied vertical section of the Patricia eastern block would have taken place, at least, from

Table 5
Calculated boiling depths for some fluid inclusions in the Patricia ore deposit. Sample depth means core sample depth below present surface. Boiling depth refers to results from the Haas diagram. The depths represent minimum depths because no evidence of boiling was observed.

	Salinity	Th	Sample depth	Boiling depth
	(wt.% NaCl)	°C	(m)	(m)
Q1	20.5	235.5	118	250
Q1	15	223.2	146	220
Q1	9.3	235.8	205	320
Q1	7	228.3	205	300
Sp1	9.1	205.3	94	145
Sp1	7.4	214.3	94	210
Sp1	5	189.5	146	120
Sp1	5.1	240.1	146	355
Sp1	3.2	190.2	150	123
Sp2	4.8	170.1	195	71
Sp2	5.6	137.9	228	25
Sp2	9.2	168.2	228	65

210 m in the shallowest level below the oxidation blanket (Sp_{2A} at 94 m deep) to 320 m close to the deepest areas drilled to date (Qz_1 at 205 m deep). However, these values represent minimum depths as Ag-rich polymetallic epithermal mineralization usually occurs in relatively deep sections (~500 m) of the epithermal environment (Hedenquist et al., 2000; Albinson et al., 2001; Camprubí and Albinson, 2006).

The difference between theoretical boiling depths and sampling depth for each inclusion also provides an approximation to the minimum amount of erosion suffered by the uplifted eastern block of the Patricia deposit. The maximum difference obtained by this method (Table 5) indicates that more than 200 m of volcano-sedimentary pile has been eroded. However, further geological evidence is needed to better constrain this value.

8.5. Sulfidation state of the Patricia ore deposit

The hydrothermal alteration, ore mineralogy and structural features of the Patricia vein system correspond to a Zn–Pb–Ag epithermal deposit mainly developed under intermediate-sulfidation (IS) conditions. The hydrothermal alteration characterized by illite ± sericite ± chlorite ± quartz is typical of IS deposits (Einaudi et al., 2003). However, according to Einaudi et al. (2003), the absence of pyrrhotite in equilibrium with pyrite or arsenopyrite suggests that the first and last stages of the Patricia deposit took place under IS conditions, although maybe close to the limit with the LS field.

The paragenetic sequence of the main ore stage consists of sphalerite, galena, chalcopyrite, pyrrhotite and Ag-bearing minerals. The sphalerite, galena and chalcopyrite deposition is usually related to IS conditions and it has been commonly described in some epithermal deposits (e.g. Hedenquist et al., 2000; Einaudi et al., 2003; Sillitoe and Hedenquist, 2003; Camprubí and Albinson, 2006; Carrillo-Rosúa et al., 2008; Bendezu and Fonboté, 2009). Moreover, the composition of the sphalerite ranges from 6 to 15 mol% FeS, which is consistent with sphalerite compositions from IS systems that range from <1 to 10 mol% FeS and locally up to 20 mol% FeS (Hedenquist et al., 2000; Einaudi et al., 2003; Simmons et al., 2005). The Ag:Au ratio of the whole-ore composition in the Patricia deposit ranges from 200 to 6000, values in accordance with IS systems where the Ag:Au ratio is always higher than 100 (Einaudi et al., 2003).

On the basis of stability fields of common sulfide species in T-fS_2 space, Einaudi et al. (2003) characterized the mineralogy of very low, low, middle, high and very high sulfidation systems. Accordingly, the whole paragenetic sequence observed in the Patricia ore deposit belongs to the intermediate sulfidation type within the stability field of chalcopyrite and pyrite (Fig. 16). Fluids of the pre-ore stage plot in an area on the T-fS_2 space characterized by moderate sulfur fugacity during pyrite and arsenopyrite deposition. During the main-ore stage, fluids progressed to lower sulfur fugacities and cooler conditions favoring the precipitation of sphalerite, galena and chalcopyrite, as well as Ag-bearing minerals. Finally, during the post-ore stage, fluids plots are higher sulfur fugacity and temperature, similar to those of the pre-ore stage, supporting the deposition of additional arsenopyrite and pyrite. The formation of kutnohorite and Ag-bearing minerals during the final post-ore stage indicates progressive cooling with an increase of pH and oxygen fugacity. Therefore, the suggested evolution for the Patricia deposit implies the existence of different pulses of fluids and fracturing

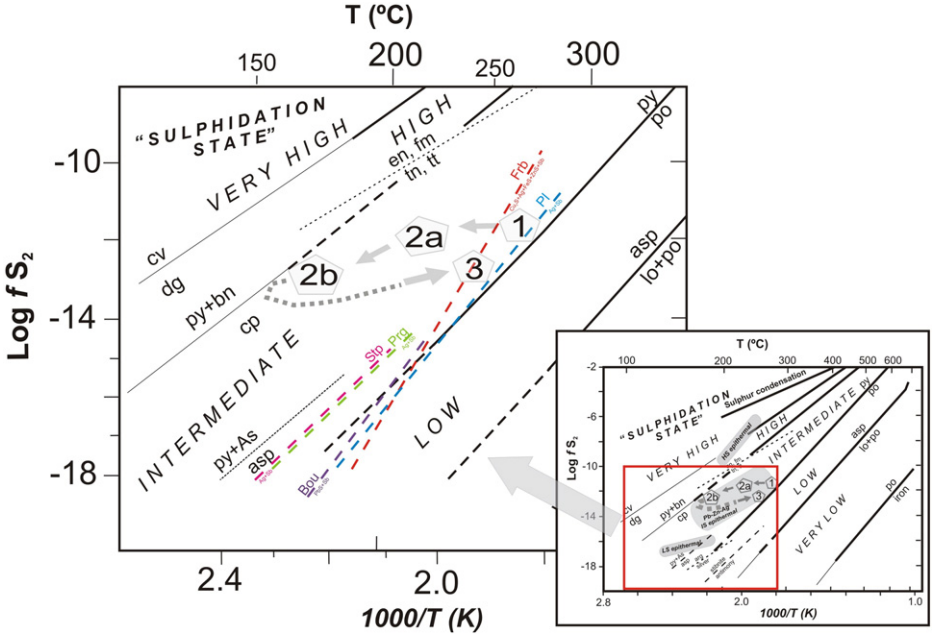

Fig. 16. Log fS_2 vs. Temperature diagram showing the inferred evolution path of the hydrothermal fluids in the Patricia ore deposit. (1) Pre-ore stage; (2a–2b) Base-metal and Ag stage and (3) Post-ore stage, based on observed mineral assemblages, fluid inclusion microthermometry and sulfide geothermometer. The diagram shows the relative sulfidation states of hydrothermal fluids in porphyry deposits and epithermal ore mineral stability fields (modified from Einaudi et al. (2003)).

supported by open-space filling and brecciation textures observed in the mineralized veins.

9. Concluding remarks

The Patricia Zn–Pb–Ag ore deposit is an intermediate sulfidation hydrothermal system associated with Cordilleran volcanism (i.e. Camprubí and Albinson, 2006). The localization of the ore bodies is controlled by extensional structures developed during the regional dominant sinistral strike-slip movement along the Domeyko fault system, at the northern extent of which the Patricia deposit is located. This overall sinistral transpressive regime created local transtensive domains with development of open spaces for hydrothermal ore deposition.

The mineralizing system was characterized by reduced fluids with pH close to neutral conditions that evolved from an initial stage characterized by saline fluids (6–22 wt% NaCl) with a minimum circulation temperature of 205 °C, likely reflecting the mixing between brine a more dilute fluid. This was followed by the main mineralization event that precipitated base metals- and Ag-bearing minerals, from a low to moderate salinity (1–9 wt.% NaCl) fluid that progressively cooled from ~250 °C to ~140 °C. The late stage is characterized by a fluid temperature increase to ~215 °C and subsequent cooling to 175 °C with no salinity variation.

The Patricia deposit is presently divided into two blocks by a set of NNW-ESE-trending reverse faults, which uplifted the eastern block and exhumed thicker and deeper parts of the deposit that exhibit IS features. At least 200 m of the host volcano-sedimentary pile has been eroded from this block. In contrast, the western block exposes a shallower part of the system where cherts, amorphous silica and jasperoids, typical of thermal spring settings, occur. So far, exploration activity has focused in the eastern part of the deposit, and little attention has been paid to the western areas as early drilling intersected veinlets with little interesting mineralization. However, the structural framework defined in this paper strongly suggests that surficial thermal spring showings in the western block could likely progress to low-sulfidation conditions at shallow depths followed by a gradual variation towards a polymetallic intermediate-sulfidation ore system at depth, equivalent to the one observed in the eastern block. Furthermore, the eastern part of the deposit most probably has an extension of the mineralized veins both at depth, as drilling has not reached the lower limit of mineralization, and towards the south beyond the ignimbrite unit, as stockwork and silicification were observed in that area during the mapping campaign included in the present work. Therefore, we propose that the Patricia ore deposit can be significantly larger than the reserves estimated at present and hidden resources are still to be discovered.

Conflict of Interest

There is no conflict of interest in our work.

Acknowledgments

This work was made possible by Herencia Resources Plc., which provided access to drill core and geologic information. Appreciation is expressed to the technical staff of Herencia Resources Plc. at the Patricia deposit, for their assistance during our studies of the deposit. A warm memory is especially devoted to Antonio Valverde, chief geologist at Paguanta project and co-author of this paper, who recently passed away. We would like to thank A. Larios and X. Llovet from the Centro Nacional de Microscopía Electrónica in the Complutense University of Madrid and from the Serveis Cientifico-tècnics of the Universitat of Barcelona, respectively, for their assistance with the electron microprobe in the chemical analyses of the minerals. We also thank B. Soutullo for their assistance with XRD from the Cristalografía y Mineralogía department in the Complutense University of Madrid. We would like to thank Dr. L. Fedele for the technical support with LA-ICP-MS analysis. This research was financially supported by the project CGL2010 – 17668 (Ministerio de Economía y Competitividad of Spain) and the company Herencia Resources Plc. Finally, we thank Franco Pirajno, editor of OGR, and two anonymous reviewers whose comments and suggestions have largely contributed to improve the paper.

References

Albinson, T., Norman, D.I., Cole, D., Chomiak, B., 2001. Controls on formation of low-sulfidation epithermal deposits in Mexico: constraints from fluid inclusion and stable isotope data. Soc. Econ. Geol. Spec. Publ. 8, 1–32.

Allmendinger, R.W., Smalley Jr., R., Bevis, M., Caprio, H., Brooks, B., 2005. Bending the Bolivian orocline in real time. Geology 33, 905–908. http://dx.doi.org/10.1130/G21779.1.

Arriagada, C., Roperch, P., Mpodozis, C., Cobbold, P., 2008. Paleogene building of the Bolivian orocline: tectonic restoration of the central Andes in 2-D map view. Tectonics 27, TC6014. http://dx.doi.org/10.1029/2008TC002269.

Barton Jr., Bethke, P.M., Roedder, E., 1977. Environment of ore deposition in the Creede Mining District, San Juan Mountains Colorado: part III. Progress toward interpretation of the chemistry of the ore-forming fluid for the OH vein. Econ. Geol. 72, 1–24. http://dx.doi.org/10.2113/gsecongeo.72.1.1.

Baumgartner, R., Fonboté, L., Vennemann, T., 2008. Mineral zoning and geochemistry of epithermal polymetallic Zn–Pb–Ag–Cu–Bi mineralization at Cerro de Pasco, Peru. Econ. Geol. 103, 493–537. http://dx.doi.org/10.2113/gsecongeo.103.3.493.

Behn, G., Camus, F., Carrasco, P., 2001. Aeromagnetic signature of porphyry copper systems in northern Chile and its geologic implications. Econ. Geol. 96, 239–248. http://dx.doi.org/10.2113/gsecongeo.96.2.239.

Bendezu, R., Fonboté, L., 2009. Cordilleran epithermal Cu–Zn–Pb (Au–Ag) mineralization in the Colquijirca District, Central Peru: deposit-scale mineralogical patterns. Econ. Geol. 104, 905–944. http://dx.doi.org/10.2113/econgeo.104.7.905.

Bodnar, R.J., 1993. Revised equation and table for determining the freezing point depression of H_2O–NaCl solutions. Geochim. Cosmochim. Acta 57, 683–684. http://dx.doi.org/10.1016/0016-7037(93)90378-A.

Bodnar, R.J., 2003. Introduction to aqueous-electrolyte fluid inclusions. In: Samson, I., Anderson, A., Marshall, D. (Eds.), Fluid inclusions: Analysis and Interpretation 32. Mineral. Assoc., Canada, pp. 81–89 (Short Course).

Bodnar, R.J., Bethke, P.M., 1984. Systematics of stretching of fluid inclusions; I, fluorite and sphalerite at 1 atmosphere confining pressure. Econ. Geol. 79, 141–161. http://dx.doi.org/10.2113/gsecongeo.79.1.141.

Bodnar, R.J., Lecumberi-Sanchez, P., Moncada, D., Steele-MacInnis, M., 2014. Fluid inclusions in hydrothermal ore deposits. In Treatise on Geochemistry, 2nd Edition, pp. 119–142.

Bouzari, F., Clark, A.H., 2002. Anatomy, evolution and metallogenic significance of the supergene ore body of the Cerro Colorado porphyry copper deposit, I Region, northern Chile. Econ. Geol. 97, 1701–1740. http://dx.doi.org/10.2113/gsecongeo.97.8.1701.

Campbell, I.H., Ballard, J., Palin, J.M., Allen, C., Faunes, A., 2006. U–Pb zircon geochronology of granitic rocks from the Chuquicamata-El Abra porphyry copper belt of northern Chile: excimer laser ablation ICP-MS analysis. Econ. Geol. 101 (7), 1327–1344. http://dx.doi.org/10.2113/gsecongeo.101.7.1327.

Camprubí, A., Albinson, T., 2006. Depósitos epitermales en México: actualización de su conocimiento y reclasificación empírica. B. Soc. Geol. Mex. 1, 27–81.

Camprubí, A., Chomiak, B.A., Villanueva-Estrada, R.E., Canals, À., Norman, D.I., Cardellach, E., Stute, M., 2006a. Fluid sources for the La Guitarra epithermal deposit (Temascaltepec district, Mexico): volatile and helium isotope analyses in fluid inclusions. Chem. Geol. 231 (3), 252–284. http://dx.doi.org/10.1016/j.chemgeo.2006.02.002.

Camprubí, A., González-Partida, E., Iriondo, A., Levresse, G., 2006b. Mineralogy, fluid characteristics, and depositional environment of the Paleocene epithermal Au–Ag deposits of the El Barqueño District, Jalisco, Mexico. Econ. Geol. 101, 235–247. http://dx.doi.org/10.2113/gsecongeo.101.1.235.

Camus, F., Dilles, J.H., 2001. A special issue devoted to porphyry copper deposits of northern Chile. Econ. Geol. 96 (2), 233–238. http://dx.doi.org/10.2113/gsecongeo.96.2.233.

Camus, F., Skewes, M.A., 1991. The Faride epithermal silver-gold deposit, Antofagasta region, Chile. Econ. Geol. 86, 1222–1237. http://dx.doi.org/10.2113/gsecongeo.86.6.1222.

Camus, F., Boric, R., Skewes, M.A., Castelli, J.C., Reichhard, E., Mestre, A., 1991. Geologic, structural, and fluid inclusion studies of El Bronce epithermal vein system, Petorca, central Chile. Econ. Geol. 86, 1317–1345. http://dx.doi.org/10.2113/gsecongeo.86.6.1317.

Canet, C., Camprubí, A., González-Partida, E., Linares, C., Alfonso, P., Piñeiro-Fernández, F., Prol-Ledesma, R.M., 2009. Mineral assemblages of the Francisco I. Madero Zn–Cu–Pb–(Ag) deposit, Zacatecas, Mexico: implications for ore deposit genesis. Ore Geol. Rev. 35, 423–435. http://dx.doi.org/10.1016/j.oregeorev.2009.02.004.

Capitanio, F., Faccenna, C., Zlotnik, S., Stegman, D., 2011. Subduction dynamics and the origin of Andean orogeny and the Bolivian orocline. Nature 480, 83–86. http://dx.doi.org/10.1038/nature10596.

Carrillo-Rosúa, J., Morales-Ruano, S., Morata, D., Boyce, A.J., Belmar, M., Fallick, A.E., Fenoll Hach-Ali, P., 2008. Mineralogy and geochemistry of El Dorado epithermal gold deposit, El Sauce district, central-northern Chile. Mineral. Petrol. 92, 341–360. http://dx.doi.org/10.1007/s00710-007-0203-7.

Catchpole, H., Kouzmanov, K., Fonboté, L., 2012. Copper-excess stannoidite and tennantite-tetrahedrite as proxies for hydrothermal fluid evolution in a zoned

cordilleran base metal district, Morococha, Central Peru. Can. Mineral. 50, 719–743. http://dx.doi.org/10.3749/canmin.50.3.719.
Chauvet, A., Bailly, L., André, A.S., Monié, P., Cassard, D., Tajada, F.L., Tuduri, J., 2006. Internal vein texture and vein evolution of the epithermal Shila-Paula district, southern Peru. Mineral. Deposita 41, 387–410. http://dx.doi.org/10.1007/s00126-006-0068-4.
Chutas, N.I., Sack, R.O., 2004. Ore genesis at La Colorada Ag–Zn–Pb deposit in Zacatecas, Mexico. Mineral. Mag. 68, 923–937. http://dx.doi.org/10.1180/0026461046860231.
Coira, B., Davidson, J., Mpodozis, C., Ramos, V., 1982. Tectonic and magmatic evolution of the Andes of northern Argentina and Chile. Earth Sci. Rev. 18, 303–332. http://dx.doi.org/10.1016/0012-8252(82)90042-3.
Cotton, W.B., 2003. Near Infrared and XRD Quantification of Porphyry Copper Alteration at Cerro Colorado and Spence, Chile Doctoral dissertation, PhD thesis University of Colorado, Boulder, USA.
Damian, G., 2003. The genesis of the base metal ore deposit from Herja. Studia UBB. Geologia 48 (1), 85–100.
Davidson, J., Mpodozis, C., 1991. Regional geologic setting of epithermal gold deposits, Chile. Econ. Geol. 86, 1174–1186. http://dx.doi.org/10.2113/gsecongeo.86.6.1174.
Dilles, J.H., Tomlinson, A.J., Martín, M.W., Blanco, N., 1997. El Abra and Fortuna Complexes: A Porphyry Copper Batholith Sinistrally Displaced by the Falla Oeste. Congreso Geológico Chileno. 8th Actas 3, pp. 1883–1887.
Echavarria, L., Nelson, E., Humphrey, J., Chávez, J., Escobedo, L., Iriondo, A., 2006. Geologic evolution of the Caylloma epithermal vein district, southern Perú. Econ. Geol. 101, 843–863. http://dx.doi.org/10.2113/gsecongeo.101.4.843.
Einaudi, M.T., Hedenquist, J.W., Inan, E.E., 2003. Sulfidation state of hydrothermal fluids: the porphyry-epithermal transition and beyond. In: Simmons, S.F., Graham, I.J. (Eds.), Volcanic, Geothermal and Ore-forming Fluids: Rulers and Witnesses of Processes Within the Earth. Soc. Econ. Geol. Geochem. Soc. Spec. Publ. 10, 285–313.
Farías, M., Charrier, R., Comte, D., Martinod, J., Hérail, G., 2005. Late Cenozoic deformation and uplift of the western flank of the Altiplano: evidence from the depositional, tectonic, and geomorphologic evolution and shallow seismic activity (northern Chile at 19°30′S). Tectonics 24, TC4001. http://dx.doi.org/10.1029/2004TC001667.
Galli, C., 1957. Las formaciones geológicas en el borde occidental de la puna de Atacama, sector de Pica, Tarapacá. Minerales 56, 14–26.
Galli, C., 1968. Carta Geológica de Chile: Cuadrángulo Juan de Morales, Provincia de Tarapacá, Escala 1:50,000: Instituto de Investigaciones Geológicas de Chile, Carta 18, (53 pp.)
Galli, C., Dingman, I., 1962. Cuadrángulos Pica, Alca, Matilla y Chacarilla, con un Estudio Sobre los Recursos de Agua Subterránea. Carta Geológica de Chile 3(2). Instituto de Investigaciones Geológicas, Provincia de Tarapacá, p. 3.
Gamarra-Urrunaga, J.E., Castroviejo, R., Bernhardt, H.J., 2013. Preliminary mineralogy and ore petrology of the intermediate-sulfidation Pallancata deposit, Ayacucho, Peru. Can. Mineral. 51, 67–91. http://dx.doi.org/10.3749/canmin.51.1.67.
García, M., Hérail, G., 2001. Comment on geochronology (Ar–Ar, K–Ar and He-exposure ages) of Cenozoic magmatic rocks from northern Chile (18–22°S): implications for magmatism and tectonic evolution of the central Andes of Wörner et al. 2000. Rev. Geol. Chile 28, 127–130. http://dx.doi.org/10.4067/S0716-02082001000100008.
Genkin, A.D., Bortnikov, N., Cabri, L.J., Wagner, F.E., Stanley, C.J., Safonov, Y.G., McMahon, G., Friedl, J., Kerzin, A.L., Gamyanin, G.N., 1998. A multidisciplinary study of invisible gold in arsenopyrite from four mesothermal gold deposits in Siberia, Russian Federation. Econ. Geol. 93, 463–487. http://dx.doi.org/10.2113/gsecongeo.93.4.463.
Goldstein, R.H., Reynolds, T.J., 1994. Systematics of fluid inclusions in diagenetic minerals: society of economic geologists and paleontologists. Short Course 31, 199.
Gröpper, H., Calvo, M., Crespo, H., Bisso, C.R., Cuadra, W.A., Dunkerley, P.M., Aguirre, E., 1991. The epithermal gold–silver deposit of Choquelimpie, Northern Chile. Econ. Geol. 86, 1206–1221. http://dx.doi.org/10.2113/gsecongeo.86.6.1206.
Haas, J.L., 1971. The effect of salinity on the maximum thermal gradient of a hydrothermal system at hydrostatic pressure. Econ. Geol. 66, 940–946. http://dx.doi.org/10.2113/gsecongeo.66.6.940.
Harambour, S., 1990. Geología pre-Cenozoica de la Cordillera de los Andes Entre las Quebradas Aroma y Juan de Morales PhD Thesis Departamento de Geología, Universidad de Chile, Santiago.
Hedenquist, J.W., Arribas Jr., A., Urien-González, E., 2000. Exploration for epithermal gold deposits. Rev. Econ. Geol. 13, 245–277.
Henley, R.W., Ellis, A.J., 1983. Geothermal systems ancient and modern: a geochemical review. Earth Sci. Rev. 19, 1–50. http://dx.doi.org/10.1016/0012-8252(83)90075-2.
Huston, D.L., Large, R.R., 1987. Genetic and exploration significance of the zinc ratio (100 Zn/(Zn + Pb)) in massive sulfide systems. Econ. Geol. 82, 1521–1539. http://dx.doi.org/10.2113/gsecongeo.82.6.1521.
Huston, D.L., Large, R.R., 1989. A chemical model for the concentration of gold in volcanogenic massive sulphide deposits. Ore Geol. Rev. 4, 171–200. http://dx.doi.org/10.1016/0169-1368(89)90017-6.
Huston, D.L., Stevens, B., Southgate, P.N., Muhling, P., Wyborn, L., 2006. Australian Zn–Pb–Ag ore-forming systems: a review and analysis. Econ. Geol. 101, 1117–1157. http://dx.doi.org/10.2113/gsecongeo.101.6.1117.
Isacks, B.L., 1988. Uplift of the central Andean plateau and bending of the Bolivian orocline. J. Geophys. Res. 93, 3211–3231. http://dx.doi.org/10.1029/JB093iB04p03211.
Jarosewich, E., Nelen, J.A., Norberg, J.A., 1980. Reference samples for electron microprobe analysis. Geostand. Newslett. 4, 43–47. http://dx.doi.org/10.1111/j.1751-908X.1980.tb00273.x.
Jasinski, A.W., 1983. Some aspects of the silver mineralization in the Hfillefors region (Bergslagen, Sweden). Mineral. Mag. 47, 507–514.
John, D.A., Hofstra, A.H., Fleck, R.J., Brummer, J.E., Saderholm, E.C., 2003. Geologic setting and genesis of the Mule Canyon low-sulfidation epithermal gold-silver deposit, north-central Nevada. Econ. Geol. 98, 425–463. http://dx.doi.org/10.2113/gsecongeo.98.2.425.
Keighin, C.W., Honea, R.M., 1969. The system Ag–Sb–S from 600 °C to 200 °C. Mineral. Deposita 4, 153–171. http://dx.doi.org/10.1007/BF00208050.
Leach, T., Corbett, G., 2008. Fluid Mixing as a Mechanism for Bonanza Grade Epithermal Gold Formation. Paper Presented at the Terry Leach Symposium, p. 17 http://dx.doi.org/10.13140/2.1.2429.1847.
Maksaev, V., 1990. Metallogenic, Geological Evolution and Thermochronology of the Chilean Andes Between Latitudes 21°and 26°S, and the Origin of Major Porphyry Copper Deposits PhD Thesis Dalhousie University, Canada.
Maksaev, V., Zentilli, M., 1999. Fission track thermochronology of the Domeyko Cordillera, northern Chile; implications for Andean tectonics and porphyry copper metallogenesis. Explor. Min. Geol. 8, 65–89.
Maksaev, V., Townley, B., Palacios, C., Camus, F., 2007. Metallic ore Deposits. In: Moreno, T., Gibbons, W. (Eds.), The Geology of Chile. The Geological Society of London, pp. 179–199.
Maronna, R.A., Martin, D.R., Yohai, V.J., 2006. Robust Statistics; Theory and Methods. Ed. Wiley, pp. 87–171.
McGuire, A.V., Francis, C.A., Dyar, M.D., 1992. Mineral standards for electron microprobe analysis of oxygen. Am. Mineral. 77, 1087–1091.
Moncada, D., Bodnar, R.J., 2012. Gangue mineral textures and fluid inclusion characteristics of the Santa Margarita Vein in the Guanajuato Mining District, Mexico. Cent. Eur. J. Geosci. 4, 300–309. http://dx.doi.org/10.2478/s13533-011-0057-8.
Moore, D.M., Reynolds, R.C., 1989. X-ray diffraction and the identification and analysis of clay minerals 378. Oxford university press, Oxford.
Mpodozis, C., Ramos, V., 1990. The Andes of Chile and Argentina. In: G. Eriksen et al. (Eds.), Geology of the Central Andes and its relation to Hydrocarbon and Mineral Resources. Circum-Pacific Council for Energy and Mineral Resources, Houston, TX. Earth Sci. Ser. 11, 59–90.
Mutchler, S.R., Fedele, L., Bodnar, R.J., 2008. Analysis Management System (AMS) for reduction of laser ablation ICPMS data. Laser-ablation-ICPMS in the earth sciences: current practices and outstanding issues. Mineralogical Association of Canada, Quebec 40, pp. 318–327.
Noble, D.C., McKee, E.H., Mégard, F., 1979. Early Tertiary "Incaic" tectonism, uplift, and volcanic activity, Andes of central Peru. Geol. Soc. Am. Bull. 90, 903–907. http://dx.doi.org/10.1130/0016-7606(1979)90<903:ETITUA>2.0.CO;2.
O'Leary, M.J., Sack, R.O., 1987. Fe–Zn exchange reaction between tetrahedrite and sphalerite in natural environments. Contrib. Mineral. Petrol. 96, 415–425. http://dx.doi.org/10.1007/BF01166687.
Pacci, D., Cáceres, R., Sayes, J., Monti, S., 1980. Inventario de Yacimientos Metálicos y no-Metálicos. I Región de Tarapacá. Tomo I-V, Antecedentes Geológicos y Mineros Básicos. Instituto de Investigaciones Geológicas.
Phillipson, S.E., Romberger, S.B., 2004. Volcanic stratigraphy, structural controls, and mineralization in the San Cristobal Ag–Zn–Pb deposit, southern Bolivia. J. S. Am. Earth Sci. 16, 667–683. http://dx.doi.org/10.1016/j.jsames.2003.11.002.
Pinto, L., Hérail, G., Charrier, R., 2004. Sedimentación sintectónica asociada a las estructuras neógenas en la Precordillera de la zona de Moquella, Tarapacá (19°15'S, Norte de Chile). Rev. Geol. Chile 31, 19–44. http://dx.doi.org/10.4067/S0716-02082004000100002.
Reich, M., Kesler, S.E., Utsunomiya, S., Palenik, C.S., Chryssoulis, S.L., Ewing, R.C., 2005. Solubility of gold in arsenian pyrite. Geochim. Cosmochim. Acta 69, 2781–2796. http://dx.doi.org/10.1016/j.gca.2005.01.011.
Reyes, A.G., 1990. Petrology of Philippine geothermal systems and the application of alteration mineralogy to their assessment. J. Volcanol. Geoth. Res. 43, 279–309. http://dx.doi.org/10.1016/0377-0273(90)90057-M.
Roel, J., Ortega, L., Piña, R., Lunar, R., 2013. Estudio Preliminar de la Mineralización de Cu-Ag de Doris, Proyecto Minero Paguanta, NE Chile MSc Thesis Complutense University of Madrid.
Romberger, S.B., 1991. Transport and Deposition of Precious Metals in Epithermal Deposits. In: Raines, G.L., Lisle, R.E., Schafer, R.W., Wilkinson, W.H. (Eds.), Geology and Ore Deposits of the Great Basin Symposium Proceedings. Geological Society of Nevada, Reno, pp. 219–232.
Sack, R.O., 2005. Internally consistent database for sulfides and sulfosalts in the system Ag2S–Cu2S–ZnS–FeS–Sb2S3–As2S3. Geochim. Cosmochim. Acta 69, 1157–1164. http://dx.doi.org/10.1016/S0016-7037(00)00468-3.
Sack, R.O., Lichtner, P.C., 2009. Constraining compositions of hydrothermal fluids in equilibrium with polymetallic ore-forming sulfide assemblages. Econ. Geol. 104, 1249–1264. http://dx.doi.org/10.2113/gsecongeo.104.8.1249.
Sayes, J., 1978. Cuadrángulos Collacagua y Laguna del Huasco, Provincia de Iquique, I Región: escala 1:100.000. Instituto de Investigaciones Geológicas de Chile, p. 43.
Schlunegger, F., Kober, F., Zeilinger, G., von Rotz, R., 2010. Sedimentology-based reconstructions of paleoclimate changes in the Central Andes in response to the uplift of the Andes, Arica region between 19 and 21°S latitude, northern Chile. Int. J. Earth Sci. 99, 123–137. http://dx.doi.org/10.1007/s00531-010-0572-8.
Seedorff, E., Dilles, J.H., Proffett, J.M., Einaudi, M.T., Zurcher, L., Stavast, W.J.A., Barton, M.D., 2005. Porphyry deposits: characteristics and origin of hypogene features. Econ. Geol. 100th Anniversary 29, 251–298.
Shamanian, G.H., Hedenquist, J.W., Hattori, K.H., Hassanzadeh, J., 2004. The Gandy and Abolhassani epithermal prospects in the Alborz magmatic arc, Semnan province, Northern Iran. Econ. Geol. 99, 691–712. http://dx.doi.org/10.2113/gsecongeo.99.4.691.
Sillitoe, R.H., 1981. Regional aspects of the Andean porphyry copper belt in Chile and Argentina. Trans. Inst. Min. Metall. 90, B15–B36.
Sillitoe, R.H., 2010. Porphyry copper systems. Econ. Geol. 105, 3–41. http://dx.doi.org/10.2113/gsecongeo.105.1.3.
Sillitoe, R.H., Hedenquist, J.W., 2003. Linkages Between Volcanotectonic Settings, ore-Fluid Compositions, and Epithermal Precious Metal Deposits. In: Simmons, S.F., Graham, I. (Eds.), Volcanic, Geothermal, and Ore-Forming Fluids: Rulers and

Witnesses of Processes Within the EarthSociety of Economic Geologists, Special Publication 10. Society of Economic Geologists. Special Publication, pp. 315–343.
Sillitoe, R.H., Perelló, J., 2005. Andean copper province: tectonomagmatic settings, deposit types, metallogeny, exploration, and discovery. Econ. Geol. 100th Anniversary, 845–890.
Simmons, S., White, N., John, D.A., 2005. Geological Characteristics of Epithermal Precious and Base Metal Deposits. In: Hedenquist, J.W., Thompson, J.F.H., Goldfarb, R.J., Richards, J.P. (Eds.), Econ Geol. 100th anniversary vol. 1905-2005, pp. 485–522
Sterner, S.M., Bodnar, R.J., 1984. Synthetic fluid inclusions in natural quartz I. Compositional types synthesized and applications to experimental geochemistry. Geochim. Cosmochim. Acta 48, 2659–2668. http://dx.doi.org/10.1016/0016-7037(84)90314-4.
Sung, Y.H., Brugger, J., Ciobanu, C.L., Pring, A., Skinner, W., Nugus, M., 2009. Invisible gold in arsenian pyrite and arsenopyrite from a multistage Archaean gold deposit: Sunrise Dam, Eastern Goldfields Province, Western Australia. Mineral. Deposita 44, 765–791. http://dx.doi.org/10.1007/s00126-009-0244-4.
Team, R.C., 2014. R: A language and environment for statistical computing. R Foundation for Statistical Computing, Vienna, Austria, 2012.
Thomas, N.A., 1967. Carta geológica de Chile: Cuadrángulo Mamiña, Provincia de Tarapacá: Instituto de Investigaciones Geológicas de Chile, carta 17, escala 1:50,000. p. 49.
Tomlinson, A.J., Blanco, N., 1997a. Structural Evolution and Displacement History of the West Fault System, Precordillera, Chile: Part 1, Synmineral History: Congreso Geológico Chileno VIII. Antafogasta, Chile, pp. 1873–1877.
Tomlinson, A.J., Blanco, N., 1997b. Structural Evolution and Displacement History of the West Fault System, Precordillera, Chile: Part 2, Postmineral History: Congreso Geológico Chileno VIII. Antafogasta, Chile, pp. 1878–1882.
Tomlinson, A.J., Blanco, N., Maksaev, V., Dilles, J.H., Grunder, A., Ladino, M., 2001. Geología de la Precordillera Andina de Quebrada Blanca–Chuquicamata, Regiones I y II (20°30′–22°30′S). Informe Registrado IR-01-20. Servicio Nacional de Geología y Minería (SERNAGEOMIN), Santiago, Chile, p. 20.
Vassileva, R.D., Atanassova, R., Kouzmanov, K., 2014. Tennantite-tetrahedrite series from the Madan Pb–Zn deposits, Central Rhodopes, Bulgaria. Miner. Petrol. 108, 515–531. http://dx.doi.org/10.1007/s00710-013-0316-0.
Victor, P., Oncken, O., Glodny, J., 2004. Uplift of the western Altiplano plateau: evidence from the Precordillera between 20° and 21°S (northern Chile). Tectonics 23, 4. http://dx.doi.org/10.1029/2003TC00151.
White, N.C., Hedenquist, J.W., 1995. Epithermal gold deposits: styles, characteristics and exploration. SEG Newslett. 23, 9–13.
Wörner, G., Seyfried, H., 2001. Reply to the Comment by M. García and G. Hérail on 'Geochronology (Ar–Ar, K–Ar and He-exposure ages) of Cenozoic magmatic rocks from northern Chile (18–22°S): implications for magmatism and tectonic evolution of the central Andes' by Wörner et al. (2000). Rev. Geol. Chile 28, 131–137. http://dx.doi.org/10.4067/S0716-02082001000100009.